

# Molecular line mapping of the giant molecular cloud associated with RCW 106 – I. $^{13}\text{CO}$

I. Bains,<sup>1\*</sup> T. Wong,<sup>1,2</sup> M. Cunningham,<sup>1</sup> P. Sparks,<sup>1</sup> D. Brisbin,<sup>3</sup> P. Calisse,<sup>1</sup>  
 J. T. Dempsey,<sup>1</sup> G. Deragopian,<sup>4</sup> S. Ellingsen,<sup>5</sup> B. Fulton,<sup>4</sup> F. Herpin,<sup>6</sup> P. Jones,<sup>2</sup>  
 Y. Kouba,<sup>1</sup> C. Kramer,<sup>7</sup> E. F. Ladd,<sup>3</sup> S. N. Longmore,<sup>1</sup> J. McEvoy,<sup>1</sup> M. Maller,<sup>1</sup>  
 V. Minier,<sup>8,9</sup> B. Mookerjea,<sup>7</sup> C. Phillips,<sup>2</sup> C. R. Purcell,<sup>1</sup> A. Walsh,<sup>1</sup>  
 M. A. Voronkov<sup>2,10</sup> and M. G. Burton<sup>1</sup>

<sup>1</sup>*School of Physics, UNSW, Sydney, NSW 2052, Australia*

<sup>2</sup>*Australia Telescope National Facility, CSIRO, PO Box 76, Epping, NSW 1710, Australia*

<sup>3</sup>*Bucknell University, Lewisburg, PA, USA*

<sup>4</sup>*Centre for Astronomy, James Cook University, Townsville, Australia*

<sup>5</sup>*School of Mathematics and Physics, University of Tasmania, Private Bag 21, Hobart, Tasmania 7001, Australia*

<sup>6</sup>*Observatoire de Bordeaux, BP 89, 33270 Floirac, France*

<sup>7</sup>*KOSMA, I. Physikalisches Institut, Universität zu Köln, Zùlpicher Strasse 77, 50937 Köln, Germany*

<sup>8</sup>*Service d'Astrophysique, DAPNIA/DSM/CEA CE de Saclay, 91191 Gif-sur-Yvette, France*

<sup>9</sup>*AIM, Unité Mixte de Recherche, CEA–CNRS–Université Paris VII, UMR 7158, CEA/Saclay, 91191 Gif sur Yvette, France*

<sup>10</sup>*Astro Space Centre, Profsovnaya St. 84/32, 117997 Moscow, Russia*

Accepted 2006 January 10. Received 2006 January 10; in original form 2005 July 6

## ABSTRACT

We present the first paper in a series detailing the results of  $^{13}\text{CO}$  observations of a  $\sim 1$  deg<sup>2</sup> region of the giant molecular cloud (GMC) complex associated with the H II region RCW 106. The  $^{13}\text{CO}$  observations are also the first stage of a multimolecular line study of the same region. These observations were amongst the first made using the new on-the-fly mapping capability of the Australia Telescope National Facility Mopra Telescope. In the configuration used, the instrument provided a full width at half-maximum (FWHM) beam size of 33 arcsec and a velocity resolution of 0.17 km s<sup>-1</sup>. The gas emission takes the form of a string of knots, oriented along an axis that extends from the north-west (NW) to the south-east (SE) of the field of the observations, and which is surrounded by a more extended, diffuse emission. We analyse the 2D integrated  $^{13}\text{CO}$  emission using the CLUMPFIND algorithm and identify 61 clumps. We compare the gas data in the GMC with the dust data provided by 21- $\mu\text{m}$  *Midcourse Space Experiment (MSX)* and 1.2-mm Swedish European Southern Observatory Submillimetre Telescope (SEST) images that we both regridded to the cell spacing of the Mopra data and smoothed to the same resolution. The  $^{13}\text{CO}$  emission is more diffuse and extended than the dust emission revealed at the latter two wavebands, which both have a much higher contrast between the peaks and the extended emission. From comparison of their centre positions, we find that only  $\sim 50$  per cent of the  $^{13}\text{CO}$  clump fits to the data are associated with any dust clumps. Using the clump fits, the total local thermodynamic equilibrium gas mass above the  $3\sigma$  level measured from the molecular data is  $2.7 \times 10^5 M_{\odot}$ , whereas that measured from the smoothed 1.2-mm SEST dust data is  $2.2 \times 10^5 M_{\odot}$ .

**Key words:** stars: formation – ISM: clouds – ISM: dust, extinction – ISM: molecules – ISM: structure – radio lines: ISM.

## 1 INTRODUCTION

A comprehensive theory of star formation that can be applied from the smallest to the largest scales and explain the low star formation

\*E-mail: ib@phys.unsw.edu.au

efficiency (SFE) remains one of the major unsolved problems of astrophysics (e.g. Klein et al. 2003; Larson 2003). The Milky Way contains  $\sim 10^9 M_{\odot}$  of cold molecular gas, which at densities of  $n_{\text{H}} \sim 10^2 \text{ cm}^{-3}$  would be expected to collapse gravitationally on a time-scale of a few Myr, far less than the age of the Galaxy. To support molecular clouds against collapse, an effective pressure due to coupling of the interstellar magnetic field with the ionized component of the gas has long been considered important (Mestel & Spitzer 1956). This coupling effectively prevents collapse in diffuse regions where the ionization fraction is high. In dense regions, the coupling is imperfect due to the drift of neutrals relative to ions (ambipolar diffusion), but is none the less strong enough to increase the collapse time-scale to  $\sim 10^7$  yr. A theory of magnetically mediated star formation has been described in detail by Shu, Adams & Lizano (1987), where high mass star formation is viewed as resulting from *supercritical* cores whose self-gravity overwhelms magnetic support, leading to rapid and efficient star formation, whereas low-mass star formation occurs in the *subcritical* regime in which collapse is slowed by magnetic fields.

Recent observations, however, have called into question this paradigm. Measurements of magnetic field strengths in dense cores, while difficult, rarely give values that are strongly subcritical, tending instead to be supercritical or at best marginally critical (Crutcher 1999; Bourke et al. 2001). In a marginally critical core, even a small amount of ambipolar diffusion should lead to rapid collapse. The high fraction of cloud cores with embedded objects (André et al. 2000) and the small age spreads in star clusters (Hartmann, Ballesteros-Paredes & Bergin 2001) also argue for relatively rapid star formation. Thus, although magnetic fields may play an important role in protostellar evolution, they may not be able (or even required) to significantly increase the star formation time-scale beyond the free-fall time.

As a result, the past few years have seen resurgence in models which propose to explain the long star formation time-scale (or equivalently, low SFE) in terms of turbulence (see review by Mac Low & Klessen 2004). The recency of these models means they are relatively untested and unconstrained by observation. The models detail how supersonic turbulence is driven on large, galactic scales (tens of parsec or more) and generates turbulence that passes to smaller scales via an energy cascade. The basic idea is that turbulence can provide global support against collapse and lead to a low overall SFE, even as locally rapid and efficient star formation occurs within the cloud. Simulations indicate that the global SFE increases as the characteristic driving scale of the turbulence increases (Klessen, Heitsch & Mac Low 2000), which suggests that spatial variations in the SFE might be used to diagnose changes in the energy injection scale. The problem of rapid decay of turbulence, even in the presence of magnetic fields, is addressed by assuming that molecular clouds are themselves transient entities, formed by shock compression of H I flows and quickly dispersed by their internal motions (Hartmann et al. 2001).

Observations of the turbulent structure of molecular clouds, combined with measures of the SFE, offer the best prospect of testing these new models. For example, by measuring the turbulence structure function across a large sample of molecular clouds and finding little variation, Heyer & Brunt (2004) conclude that energy injection from embedded massive stars may be relatively unimportant. Comparison of observations and numerical simulations (Ossenkopf & Mac Low 2002; Brunt 2003) has also led to the conclusion that the energy injection occurs on large scales compared with the dimensions of a typical giant molecular cloud (GMC). However, such observations have tended to rely on a single molecular gas tracer,

such as  $^{12}\text{CO}$ , and have not included observations of the young stellar content to assess the SFE. In addition, a low-density tracer such as  $^{12}\text{CO}$  will have a much wider distribution than higher density tracers and primarily only provides a measure of the lower density molecular gas that lies between the denser cores.

As pointed out by Ballesteros-Paredes & Mac Low (2002), useful constraints on the driving strengths of turbulence in molecular clouds can be provided by observing the same regions in several emission lines that trace different densities. In the case of weakly driven turbulence, a low-density tracer such as  $^{13}\text{CO}$  will have a much wider distribution than a high-density tracer such as CS. In contrast, strongly driven turbulence results in a spatial distribution that is similar for both high- and low-density tracers, because there are more regions of both higher density where both tracers can be excited, and lower density where neither is excited.

Therefore, with the aims of investigating the role played by turbulence in star formation, testing the newly available turbulence models and providing the requisite observational constraints for them, we have instigated a programme of observations with the Mopra radiotelescope, specifically focusing on a GMC complex situated in the southern Galactic plane. The novel aspect of this programme lies in mapping the same GMC in several millimetre molecular line transitions that are sensitive to a range of density conditions, from  $\sim 10^2$  to  $10^5 \text{ cm}^{-3}$ , thus enabling the investigation of turbulence over a range of scales. The programme commenced in the winter 2004 observing season with observations in  $^{13}\text{CO}$ , a relatively low critical density tracer of  $n_{\text{crit}} \sim 10^2 \text{ cm}^{-3}$ , which maps out the total extent of the molecular gas present.

### 1.1 The target

The GMC complex that is the target of this project is associated with the H II region RCW 106 and spans a  $1^{\circ}2 \times 0^{\circ}6$  region on the sky. We informally call this project the ‘Delta Quadrant Survey’ because the GMC is situated in the fourth quadrant of the Milky Way, in the southern Galactic plane, roughly centred on  $l \sim 333^{\circ}$ ,  $b \sim -0^{\circ}5$  or  $\alpha_{\text{J2000}} = 16^{\text{h}}21^{\text{m}}$ ,  $\delta_{\text{J2000}} = -50^{\text{d}}30^{\text{m}}$ . Henceforth, we will refer to it as the G333 cloud. The velocity structure of the G333 cloud is centred on  $v_{\text{LSR}} \sim -50 \text{ km s}^{-1}$  with a width of  $\sim 30 \text{ km s}^{-1}$ . In Section 3.1, we detail how a number of clouds at discrete velocities are visible in the Mopra bandpass along the line of sight to the G333 region, hence for simplicity we will also refer to our main target of interest as ‘the GMC’ to distinguish it from the other spatially smaller velocity features. At a distance of 3.6 kpc (Lockman 1979), the G333 complex spans  $90 \times 30$  pc; we discuss the distance estimate further in Section 3.1. The GMC contains a varied sample of molecular regions with a range of high mass star forming clouds, bright H II regions, *IRAS* and *Midcourse Space Experiment (MSX)* sources, all of which are surrounded by regions of diffuse atomic and molecular gas.

The GMC forms part of the Galactic Molecular Ring (e.g. Simon et al. 2001) that encircles the Galactic centre at a radius of 3–5 kpc. *MSX* images (e.g. Fig. 1) of the region reveal a large-scale emission structure that is linear and extends over a degree across the sky. By eye, this large-scale emission can be separated into six or so distinct knotty regions, each of which displays much clumping and arc-like filamentary and wispy features. In far-infrared (FIR; Karnik et al. 2001) and 1.2-mm (Mookerjee et al. 2004) dust maps, the linear clumpiness of the region becomes more apparent. Some of these dust clumps harbour OB associations capable of producing ultraviolet (UV) photons that ionize their immediate environs within their natal GMC, resulting in regions of compact radio emission.

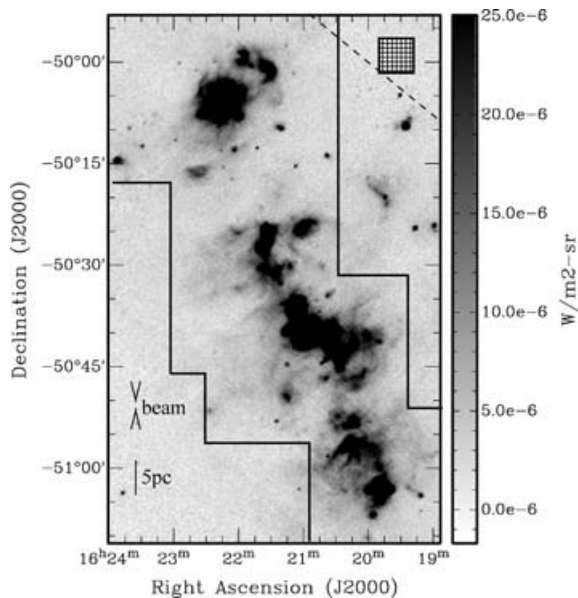


**Figure 1.** 21- $\mu\text{m}$  MSX image of the region observed in  $^{13}\text{CO}$  by the Mopra Telescope, with a FWHM beam width of 33 arcsec. The hatched box illustrates the dimensions of the individual  $5 \times 5$  arcmin $^2$  raster maps, 94 of which were used to cover the region enclosed by the black border lines shown. The saturated grey-scale stretch was chosen to illustrate the extent of the fainter, diffuse dust emission in the field. The 33-arcsec Mopra beam size is indicated, as is a 5-pc length-scale bar for a distance of 3.6 kpc. The approximate position of the Galactic plane is indicated by the dashed line.

RCW 106 as well as other radio-detected H II regions in the GMC include IRAS 16158–5055, 16172–5028, 16177–5018, G333.0–0.4 and G333.6–0.2 (e.g. Shaver & Goss 1970; Retallack & Goss 1980, see Fig 3). FIR emission, such as that imaged by Karnik et al. (2001), can arise from the reradiation of energy that is acquired by the dust surrounding OB stars after it is heated by the stellar UV photons. Where conditions are favourable for the escape of visible photons, H II regions can be detected optically. Both G333.6–0.2 (Russeil et al. 2005) and RCW 106 display optical H $\alpha$  emission; indeed, RCW 106 itself was discovered in the H $\alpha$  survey of Rodgers, Campbell & Whiteoak (1960). The 8- $\mu\text{m}$  MSX band, in which the GMC is bright, is sensitive to emission from polycyclic aromatic hydrocarbons (PAHs) that in star forming regions arise in photodissociation regions (PDRs) between H II regions and the surrounding neutral molecular material.

Molecular line emission from the GMC surrounding RCW 106 was first detected by Gillespie et al. (1977) in  $^{12}\text{CO}$  ( $J = 1-0$ ), and this emission was later mapped with a 9-arcmin beam in the survey of Bronfman et al. (1989). OH, H $_2\text{O}$  and CH $_3\text{OH}$  maser lines are also tracers of high mass star formation, and these have been detected from various sources in the region (e.g. Batchelor et al. 1980; Caswell, Haynes & Goss 1980; Caswell et al. 1995). Various pointed molecular line observations within the region have been made, such as those previously mentioned and the many species observed by Mookerjea, Kramer & Burton (2005). However, with the exception of the low-resolution observations of Bronfman et al. (1989) and the  $^{12}\text{CO}$  NANTEN telescope survey (e.g. Mizuno et al. 2003), to date no systematic, multimolecular-line mapping survey of this region, such as that involved in our programme, has taken place.

Mass estimates of the G333 complex have been made possible through the observations of optically thin dust emission by Karnik

et al. (2001) and Mookerjea et al. (2004). Karnik et al. (2001) made a FIR 150- and 210- $\mu\text{m}$  dust study of the region using their balloon-borne 1-m telescope with a resolution of  $\sim 1$  arcmin. To illustrate the degree of optical thinness of the dust at these wavelengths, we note that the peak optical depth (Karnik et al. 2001) measured at 210  $\mu\text{m}$  was 0.10. Using the canonical gas:dust ratio of 100, they measure a total GMC mass of  $1.8 \times 10^5 M_{\odot}$ . The 1.2-mm cool dust continuum emission from the region was imaged by Mookerjea et al. (2004) using SEST Imaging Bolometer Array (SIMBA) on the SEST with a resolution of 24 arcsec. Using the same gas:dust ratio, they estimated a total mass of  $\sim 10^5 M_{\odot}$ , consistent with that of Karnik et al. (2001). As molecular clouds typically have masses of the order of  $10^2$ – $10^4 M_{\odot}$  and those of GMCs are  $10^4$ – $10^6$  (e.g. Mac Low & Klessen 2004), these mass estimates, along with the extended size of the region, validate our naming of this complex as a GMC.

## 1.2 This paper

In this paper, we introduce the project and present a preliminary analysis of the  $^{13}\text{CO}$  data, based on our analysis of the 2D integrated  $^{13}\text{CO}$  emission from the GMC. The organization of the paper is as follows. In Section 2, we describe the observing technique, including the new ‘on-the-fly’ (OTF) raster mapping capability of the Mopra telescope. In Section 3, we examine the structure of the total intensity  $^{13}\text{CO}$  emission and compare it with the 21- $\mu\text{m}$  dust structure revealed by SPIRIT III (the Spatial Infrared Imaging Telescope) aboard the MSX satellite and the 1.2-mm Swedish European Southern Observatory (ESO) Submillimetre Telescope (SEST) SIMBA dust continuum data of Mookerjea et al. (2004). In Section 4, we present an analysis of the 2D  $^{13}\text{CO}$  emission structure by decomposing it into clumps using the CLUMPFIND algorithm of Williams et al. (1994) and, finally, in Section 5 we summarize the findings.

## 1.3 Outline of future work

Here, we briefly outline some work in progress that will appear in subsequent publications and will provide various independent means of investigating the role of turbulence in star formation. We are currently performing the detailed analysis of the full 3D spatio-kinematic  $^{13}\text{CO}$  data set, employing the 3D GAUSSCLUMPS and CLUMPFIND (Williams et al. 1994; Kramer et al. 1998) algorithms to decompose the molecular emission structure into clumps, as defined by their individual brightness distribution and velocity structure. This will enable a study of the  $^{13}\text{CO}$  clump linewidths, virial masses and boundedness, and we will repeat the analysis for the other molecular lines we are in the process of observing, which include C $^{18}\text{O}$ , CS and C $^{34}\text{S}$ . The clump scaling properties and mass spectral indices obtained in this way will give information on the nature of the turbulence present (see e.g. Klessen 2002, and also Section 4.1.2) as well as the general cloud properties.

We will also present a derivation of the distribution of column densities in this GMC by combining recently obtained C $^{18}\text{O}$  Mopra data with the  $^{13}\text{CO}$  and mm continuum imaging discussed in this work. The combination of column density and velocity information will provide constraints on the density probability distribution function (PDF), a fundamental property of turbulent gas (Vázquez-Semadeni & García 2001). In particular, we should be able to test for similarity in the structure functions of projected density and velocity as found by Padoan et al. (2003) in Taurus and Perseus, as well as examine the slopes of intensity power spectra in velocity slices of varying thickness to probe the turbulent energy spectrum (Lazarian & Pogosyan 2000).

In addition to the lower-density tracer CO isotopomers, we are mapping the GMC region in higher density tracers, which so far include CS and C<sup>34</sup>S mapping using the Mopra antenna and NH<sub>3</sub> imaging using the Australia Telescope Compact Array (ATCA) to provide a check on the PDF derived from column density tracers. Moreover, a comparison of low- and high-density tracers will allow us to probe the driving strength of the turbulence using diagnostics such as thin–thick slicing of datacubes and the spectral correlation function (Rosolowsky et al. 1999). An important caveat is that most of the detected high-density gas may occur in collapsed regions, but even then the line data might serve as a useful probe of energy injection into the cloud.

All of the above gas tracers will be compared with recent star formation probed in the mid-infrared by the *Spitzer* Galactic Legacy Infrared Mid-Plane Survey Extraordinaire (GLIMPSE) survey, to assess how the SFE varies as a function of location within the cloud, as might occur if triggering by external pressure is important for initiating star formation.

## 2 OBSERVATIONS AND DATA PROCESSING

The Mopra Telescope is operated by the Australia Telescope National Facility (ATNF) and is situated next to the Warrumbungles National Park, near Coonabarabran, NSW. It is a centimetre- and millimetre-wavelength antenna, having a full width at half-maximum (FWHM) beam size of  $\sim 33$  arcsec at 110 201.353 MHz, and the rest frequency of the <sup>13</sup>CO J = 1–0 transition.

The angular extent of the G333 observations is illustrated within the borders marked in the 21- $\mu$ m *MSX* image in Fig. 1. This area was chosen on the basis of available *MSX* images, and we attempted to encompass the integrated <sup>13</sup>CO emission down to a level which is  $\sim 10$  per cent of the peak, within the limits set by the available observing time. As no <sup>13</sup>CO map of this region was already in existence, we determined where the <sup>13</sup>CO 10 per cent level is simply by starting our observations in the regions of bright *MSX* emission and extending the field of the observations systematically outwards until the  $\sim 10$  per cent level was approached.

For the purpose of observation, the region to be mapped was divided into a grid of individual fields of extent  $300 \times 300$  arcsec<sup>2</sup> and with centre pointings separated by 285 arcsec in RA and Dec. The extent of the observing grid and the size of an individual field are shown in Fig. 1, overlaid on the 21- $\mu$ m *MSX* image of the region. The centre pointing separations ensured that the adjacent fields overlapped by 15 arcsec, about half the beam size, to ensure full coverage of the region and to facilitate the mosaicing of the data in the reduction stages. The observing mode was ‘OTF’ (follow the links from <http://www.narrabri.atnf.csiro.au/> for more details) raster scanning whereby individual raster maps were made of each field with the telescope continually scanning at a rate of 3.5 arcsec s<sup>-1</sup> and averaging data over a 2-s cycle time which gave an optimum data collection rate whilst not smearing the output. The scan rows (columns) had a 10-arcsec spacing, with a 7-arcsec spacing between the spectra along a row (column) and 46 spectra per row (column). Each  $300 \times 300$  arcsec<sup>2</sup> raster map comprised 31 rows (columns), resulting in  $\sim 1400$  spectra per map. Each map took  $\sim 70$  min to complete and with  $\sim 10$  min for calibration and pointing overheads, seven maps could be obtained per transit of the Galactic centre in favourable weather conditions.

The data were observed over  $\sim 10$  weeks during an intermittent observing period that spanned from 2004 July to 2004 October. Initially, a first pass (Grid 1) of the whole region was made with the telescope scanning mode in the RA direction, and a total of 93

fields were mapped. A second pass (Grid 2) was then made with field centres offset by 1 arcmin north (N) and 1 arcmin east (E) from those in Grid 1 and with the scan direction orthogonal to that used in the complementary fields in Grid 1. The offset was used to minimize any spurious ‘edge effects’ being introduced at the field boundaries. The target fields were referenced to an OFF (emission-free) position centred on  $\alpha_{J2000} = 16:27$ ,  $\delta_{J2000} = -51:30$  in order to perform the sky subtraction. The telescope tracked the OFF position for 22 s each time it finished an RA (or Dec.) scan row (column) along a given field. A  $T_{\text{sys}}$  measurement was made with the paddle (chopper wheel) after every 11 rows (columns).

The correlator was configured with 1024 channels over a 64-MHz bandwidth, which provided a velocity resolution of 0.17 km s<sup>-1</sup> channel<sup>-1</sup> over a useable velocity bandwidth of  $\sim 120$  km s<sup>-1</sup>. The observing was set up so that the central channel corresponded to  $-50$  km s<sup>-1</sup>, the velocity at which the emission from the GMC complex is centred. Throughout this work, velocities are given in the radio convention, in terms of  $v_{\text{LSR}}$ , that is, with respect to the kinematic local standard of rest (LSR).

The observations were made in dual orthogonal linear polarization mode. In the case of the Mopra antenna, the dual polarizations are termed ‘polarization A’ and ‘polarization B’, and this is simply the terminology for the two IF channels used in collecting the data; it does not refer to any physical polarization, per se. The pointing of the antenna was checked in between observations of each field by tuning polarization B to the SiO maser frequency 86 243.442 MHz and pointing on the nearby late-type stellar sources AH Sco or IRSV 1540. The pointing errors were typically below 10 arcsec. The Mopra beam has been characterized (see Ladd et al. 2005) and is now regularly monitored. The beam comprises a central component which contains the majority of the power and a surrounding ‘error beam’ which is below the 10 per cent level. The main beam brightness temperature  $T_{\text{MB}}$  and antenna temperature  $T_{\text{A}}^*$  are related by the antenna efficiency  $\eta_{\nu}$  at frequency  $\nu$  such that  $T_{\text{MB}} = T_{\text{A}}^*/\eta_{\nu}$ . In the 2004 Mopra observing season, Ladd et al. (2005) found that  $\eta_{115\text{GHz}} = 0.55$ . Standard <sup>13</sup>CO spectra of the molecular cloud sources M17 and Orion KL were taken throughout the observing period to monitor the instrumental flux density calibration. The error in the flux density scale is  $\sim 10$  per cent. The polarization B <sup>13</sup>CO data are noisier, with typical recorded values of  $T_{\text{sys}}$  (in  $T_{\text{A}}^*$ ) during the observations of 280 K (polarization A) and 330 K (polarization B).

The data were reduced using the LIVEDATA and GRIDZILLA packages available from the ATNF and adapted from the versions used to reduce the Parkes multibeam H I data from the southern Galactic Plane Survey of e.g. McClure-Griffiths et al. (2001) and Kavars et al. (2003). LIVEDATA performs a bandpass calibration for each row using the preceding OFF scan and then fits a user-specified polynomial to the spectral baseline. GRIDZILLA grids the data according to user-specified weighting and beam parameter inputs. To grid the data, we used a cell size of  $12 \times 12$  arcsec<sup>2</sup>. The data were weighted by the relevant  $T_{\text{sys}}$  measurements. The typical rms noise per 0.17 km s<sup>-1</sup> channel was 0.30 K ( $T_{\text{A}}^*$ ) in the Grid 1 fields and 0.36 K for those in Grid 2.

## 3 RESULTS

### 3.1 Velocity structure

As might be expected for such a ubiquitous species, <sup>13</sup>CO emission was detected over much of the available bandpass. The spatially averaged spectrum of the emission from the whole region observed

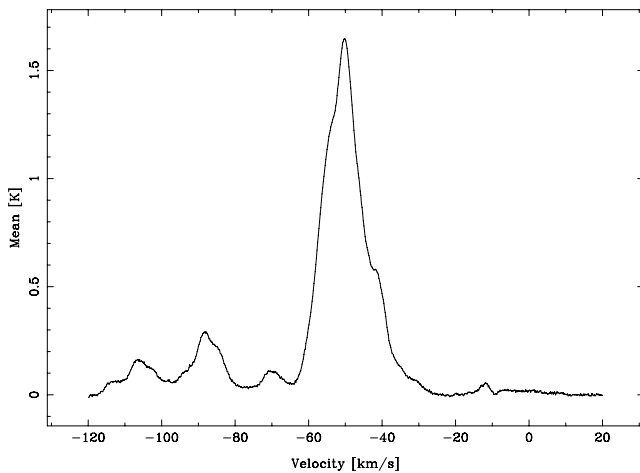


**Figure 2.** The mean velocity profile of the  $^{13}\text{CO}$  emission averaged over the full spatial extent of the Mopra observations. The ordinate is in terms of  $T_{\text{A}}^*$ . Five distinct velocity features are apparent in the range sampled by the bandpass.

is shown in Fig. 2, where five distinct velocity features are apparent. The emission attributed to the GMC is that of the brightest, broadest velocity feature, centred on  $\sim -50 \text{ km s}^{-1}$ , which itself appears to be comprising at least three velocity components. The

emission from the GMC is spatially extensive (Section 3.2) and is found contiguously over a velocity range that spans from  $-65$  to  $-35 \text{ km s}^{-1}$ .

The other four discrete velocity features apparent in Fig. 2 are centred on  $-10$ ,  $-70$ ,  $-90$  and  $-105 \text{ km s}^{-1}$ . We used the Galactic rotation curve given by Brand & Blitz (1993) to plot the kinematic distance versus the LSR velocity at a Galactic longitude of  $333^\circ.2$ , roughly the position of the GMC centre. We also plotted the upper and lower error bounds assuming a  $\pm 20 \text{ km s}^{-1}$  uncertainty in the true rotational velocity. These uncertainties introduced an error of  $\sim 1 \text{ kpc}$  at each velocity, but we found that for clouds at  $-10$ ,  $-50$ ,  $-70$ ,  $-90$  and  $-105 \text{ km s}^{-1}$  the associated near kinematic distances are 1, 3.5, 4.5, 5.5 and 6.5 kpc, respectively.

### 3.2 Integrated emission

A total intensity image of the  $^{13}\text{CO}$  emission integrated over the full bandpass and clipped at the  $3\sigma$  level of  $0.55 \text{ K channel}^{-1}$  is shown in Fig 3. In this image, the  $^{13}\text{CO}$  emission takes the form of a linear series of dense knots, extending from the north-west (NW) to the south-east (SE) of the observed field and surrounded by more diffuse, extended patches and filaments of emission. The main axis of the knots is at position angle  $\sim 25^\circ$  measured E from N. With respect to the Galactic plane, this main axis is inclined by  $25^\circ$  such that the lesser Galactic longitudes are at a lower latitude (see Fig. 1). The brightest  $^{13}\text{CO}$  feature with a peak integrated emission of

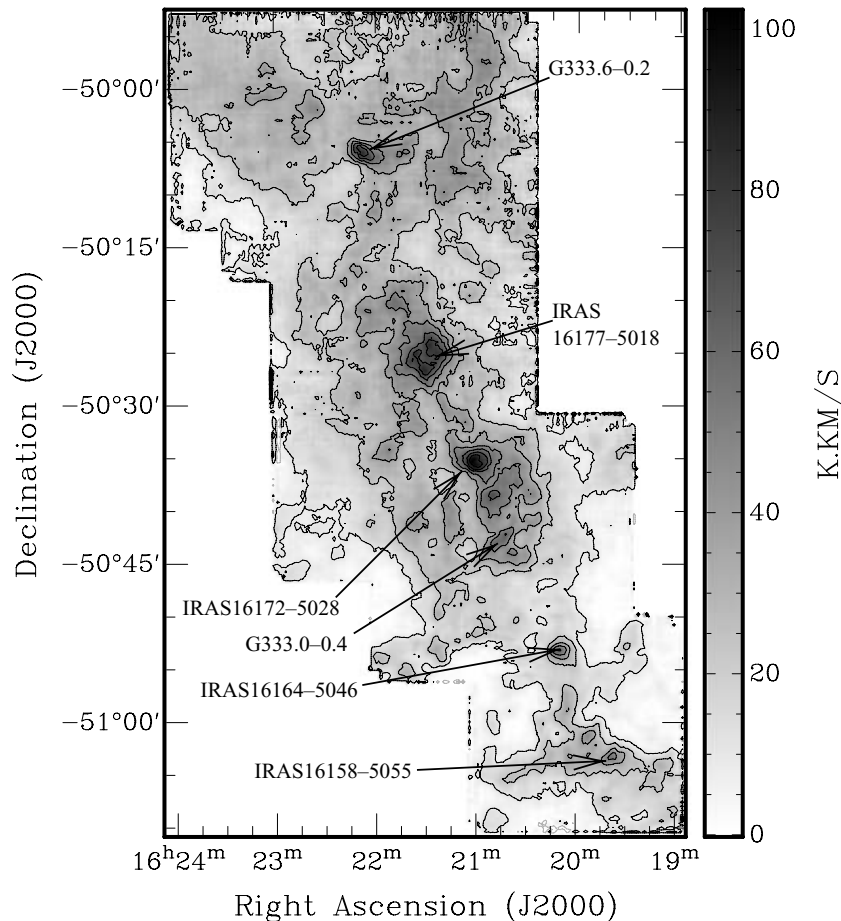


**Figure 3.** The total  $^{13}\text{CO}$  emission integrated over the full bandpass from  $-120$  to  $20 \text{ km s}^{-1}$  and clipped at the  $3\sigma$  rms level of  $0.55 \text{ K channel}^{-1}$ . The scale bar indicates the range of the integrated emission displayed, from 0 to the peak brightness of  $102 \text{ K km s}^{-1}$ , and the contours are plotted at 10 per cent levels of the peak. The temperatures are in terms of  $T_{\text{A}}^*$ . The brighter molecular regions are in proximity to some of the H II regions in the field and these are indicated.

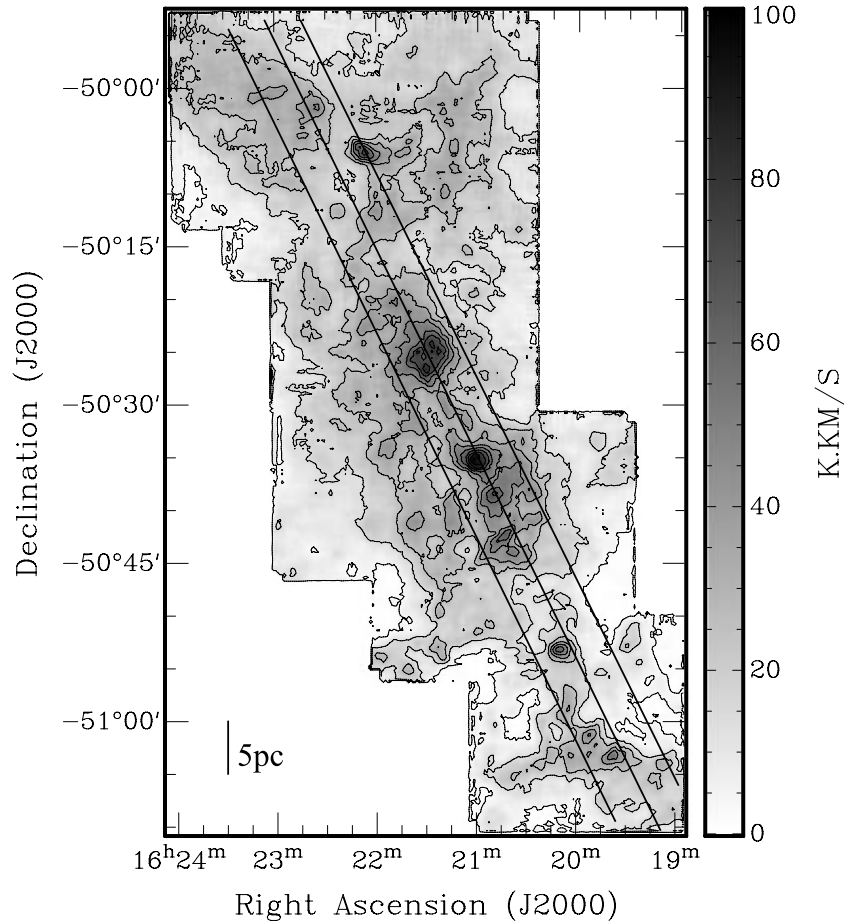


**Figure 4.** The total  $^{13}\text{CO}$  emission attributed to the GMC complex integrated over the velocity range  $-65$  to  $-35$   $\text{km s}^{-1}$  and clipped at the  $3\sigma$  rms level of  $0.55$   $\text{K channel}^{-1}$ . The scale bar indicates the range of the integrated emission displayed, from 0 to the peak brightness of  $101$   $\text{K km s}^{-1}$ , and the contours are plotted at 10 per cent levels of the peak. The temperatures are in terms of  $T_{\text{A}}^*$ . The parallel black lines show the approximate positions of the cuts used in making the pv-arrays shown in Fig. 8.

$100$   $\text{K km s}^{-1}$  (in  $T_{\text{A}}^*$ ) is found in proximity to the H II region IRAS 16172–5028 at position  $\alpha_{\text{J2000}} = 16:21:00$ ,  $\delta_{\text{J2000}} = -50:35:21$ .

The zeroth-order moment image of the  $^{13}\text{CO}$  emission attributed to the GMC alone, integrated over its  $-65$  to  $-35$   $\text{km s}^{-1}$  velocity extent and clipped at the  $3\sigma$  per channel level, is given in Fig. 4. The structure of the emission is very similar to that seen in Fig. 3 and illustrates how the brightness distribution from the GMC dominates over the other discrete velocity features found in the field.

In Fig. 5, we show the individual zeroth-order moment images of these other velocity features that are centred on  $-10$ ,  $-70$ ,  $-90$  and  $-105$   $\text{km s}^{-1}$ . These images were summed over respective velocity ranges of  $-16$  to  $-9$ ,  $-78$  to  $-65$ ,  $-99$  to  $-78$  and  $-110$  to  $-100$   $\text{km s}^{-1}$  and were clipped at  $0.55$   $\text{K channel}^{-1}$  whilst being constructed. In general, the emission from these other velocity features is of a much lower level than that found in the GMC, with knotty spatial distributions that are scattered over large areas without much contiguous structure.

In order to compare the  $^{13}\text{CO}$  data with other recent and pertinent observations, we obtained the 1.2-mm data of Mookerjea et al. (2004) and the 21- $\mu\text{m}$  *MSX* image of the same region. Of the four *MSX* bands available (8.3, 12.1, 14.7 and 21.3  $\mu\text{m}$ ), the shorter wavelength bands contain PAHs emission lines whereas the longer wavebands are dominated by the thermal emission from dust (Kraemer et al. 2003). Hence, for the purpose of tracing the dust

structure, the 21- $\mu\text{m}$  image is most relevant. The 1.2-mm emission is optically thin and traces the cool dust surrounding the sites of star formation, while the 21- $\mu\text{m}$  emission arises from warmer dust, is generally optically thick and is subject to self-absorption from cooler foreground dust. Only the millimetre dust emission is therefore suitable for making mass estimates.

The resolutions of the SEST and *MSX* images were 24 and 18 arcsec, respectively. For comparison, we regridded the dust data sets to the same cell spacing as the  $^{13}\text{CO}$  Mopra data and smoothed them to the same resolution, i.e. a  $12 \times 12$  arcsec<sup>2</sup> grid spacing and 33 arcsec beam size. In Figs 6 and 7, we show grey-scales of the resulting *MSX* and SEST images overlaid with the higher contours of the integrated  $^{13}\text{CO}$  GMC emission from Fig. 4 (we omit the lower contours for the sake of clarity). It is immediately obvious that the GMC shows a similar large-scale emission structure at each of the wavelengths in the form of the NW–SE string of clumpy emission visible in Fig. 4. Many of these knotty features are seen at all three wavelengths, for example, the emission associated with IRAS 16164–5046 at  $\sim 16:20$ ,  $-50:53$ . All of the brightest  $^{13}\text{CO}$  knots (above the 50 per cent contour) appear to be associated with bright SEST dust peaks. A few dust knots show a more pronounced contrast than their counterparts in the  $^{13}\text{CO}$  image: for example, those at  $\sim 16:22:15$ ,  $-50:12$ ;  $16:21:15$ ,  $-50:10$  and  $16:21:35$ ,  $-50:40$ . The mid-IR *MSX* data show more differences with the Mopra data,

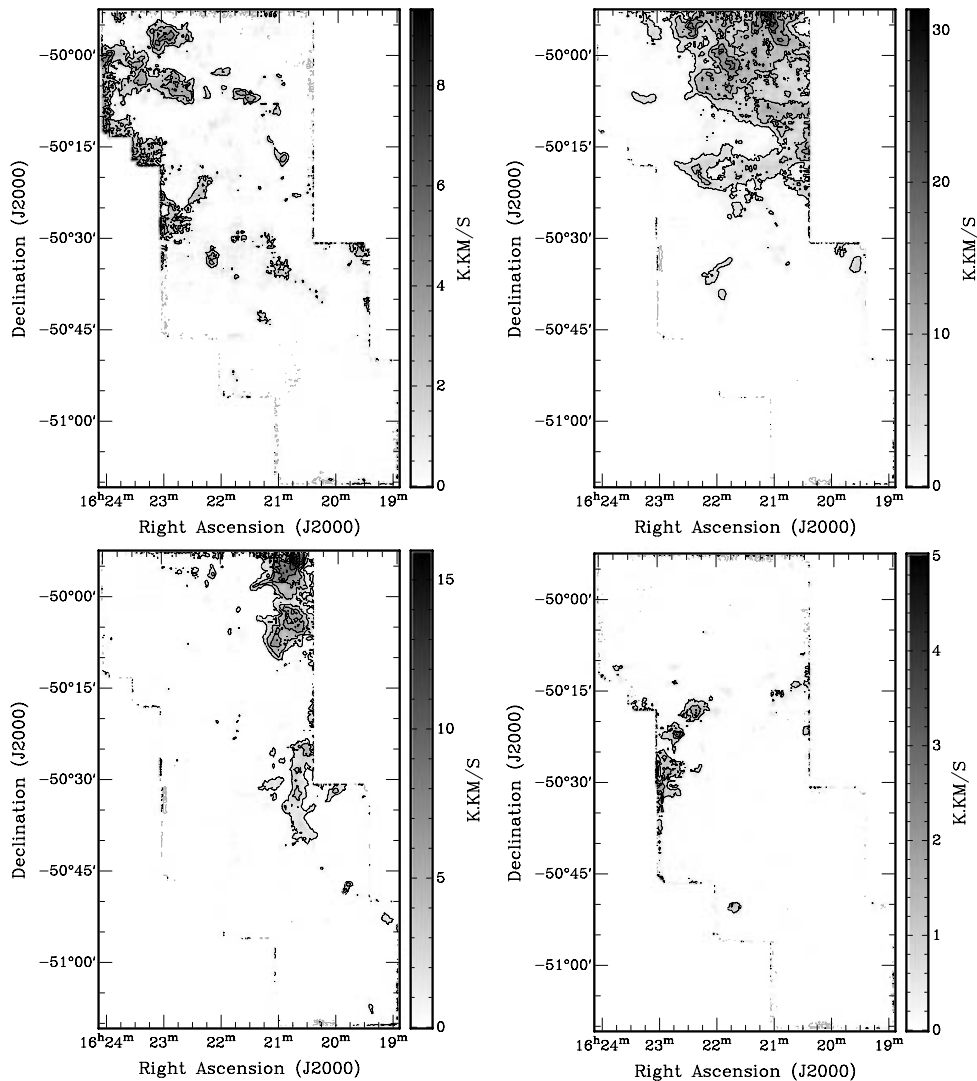


**Figure 5.** The integrated emission from the discrete velocity features centred on (and summed over): top left  $\sim -105 \text{ km s}^{-1}$  ( $-110$  to  $-100 \text{ km s}^{-1}$ ); top right  $\sim -90 \text{ km s}^{-1}$  ( $-99$  to  $-78 \text{ km s}^{-1}$ ); bottom left  $\sim -70 \text{ km s}^{-1}$  ( $-78$  to  $-65 \text{ km s}^{-1}$ ); bottom right  $\sim -10 \text{ km s}^{-1}$  ( $-16$  to  $-9 \text{ km s}^{-1}$ ). The scale bars range from  $0 \text{ K km s}^{-1}$  to the peak brightness on each image (respectively 10, 31, 16 and  $5 \text{ K km s}^{-1}$ ), and the contours are plotted at 10 per cent levels of the respective peak brightnesses.

with peaks of  $21\text{-}\mu\text{m}$  emission where no corresponding  $^{13}\text{CO}$  knots are seen, for example the complex of mid-IR knots centred around  $16:21, -50:40$ , the mid-IR knot at  $\sim 16:20:15, -50:56$  and also that at  $\sim 16:21:30, -50:02$ . There is a large, bright mid-IR knot at  $\sim 16:20:30, -50:40$  that in the  $^{13}\text{CO}$  data appears as a group of smaller, fainter, fragmented knots. Both the SEST and *MSX* dust data show a larger range in brightness than the  $^{13}\text{CO}$  data; the  $^{13}\text{CO}$  emission is clearly more diffuse than that of the dust, with less contrast between the peaks and the more extended emission. We note that the lack of low-level brightness structure in the dust data could be due to the sensitivity limitations of the observations.

The more extended distribution of  $^{13}\text{CO}$  relative to mm continuum emission suggests that high-density gas may be strongly confined to high column density regions. Such a conclusion must be verified with future observations of high-density molecular tracers, as the mm continuum emission does not strictly trace volume density – rather, it is a temperature-weighted measure of column density. None the less, previous studies suggest that continuum peaks are well correlated with high-density tracers (e.g. Tafalla et al. 2002), and

that high column density is generally a prerequisite for dense core formation (e.g. Johnstone, Di Francesco & Kirk 2004; Hatchell et al. 2005). If this is the case, then the lack of high-density gas in the outer parts of the cloud suggests that turbulent driving is weak in these regions, or that pressure from a weak magnetic field acts to smooth out strong density fluctuations (cf. Ballesteros-Paredes & Mac Low 2002). Either conclusion would argue against models that invoke turbulence rather than magnetic fields to prevent efficient star formation. However, it is possible that the SEST observations were insensitive to the high-density filamentary structure that would be generated by turbulence. A more careful analysis, taking into consideration the sensitivity limits of the observations, will appear in future work.

### 3.3 Position–velocity arrays

In Fig. 8, we show the pv-arrays taken from the  $^{13}\text{CO}$  data cube across the velocity range attributed to the GMC only. The positions of the slices used to make the arrays are illustrated in Fig. 4 and

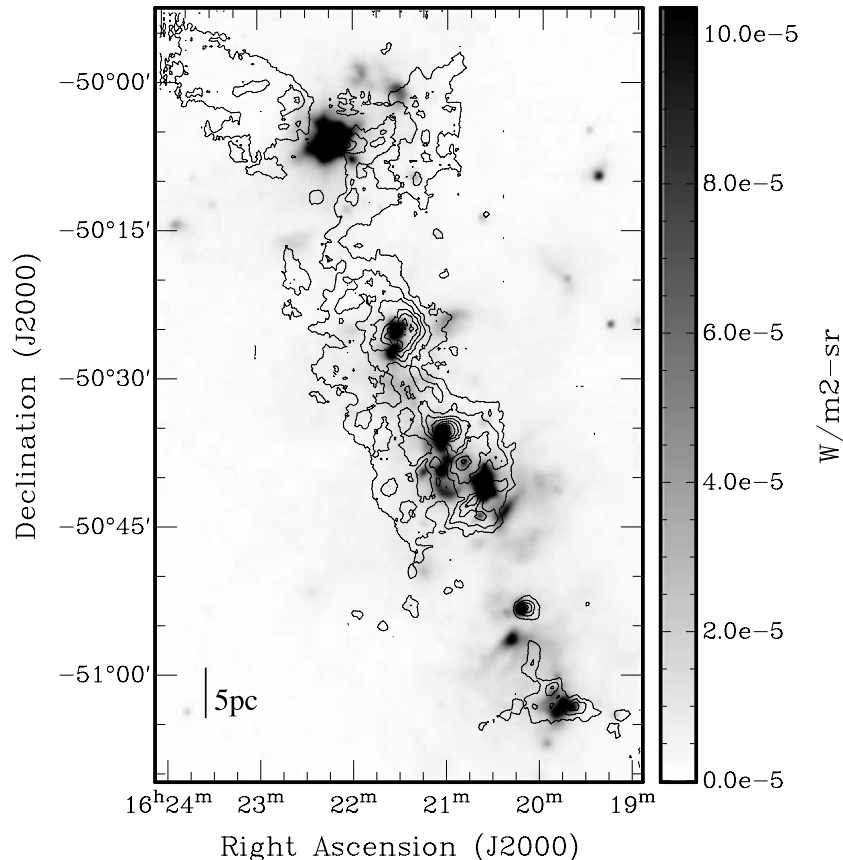


**Figure 6.** Grey-scale plot of the 21- $\mu\text{m}$  *MSX* image that has been regridded to the Mopra  $^{13}\text{CO}$  cell spacing and smoothed to the same resolution, overlaid with contours of the integrated  $^{13}\text{CO}$  emission from the GMC, starting from 30 per cent of the peak and increasing in steps of 10 per cent (see Fig. 4). The scale bar indicates the displayed stretch in 21- $\mu\text{m}$  flux density; the actual peak is  $3 \times 10^{-3} \text{ W m}^{-2} \text{ sr}^{-1}$ .

were chosen to pass along, or parallel to, the main axis of emission in the field. This axis is  $\sim 25^\circ$  measured E from N and is defined by the knotty string of  $^{13}\text{CO}$  emission apparent in Fig. 4.

In each array, discrete clumps of emission of typical angular extent of a few arcmin are seen surrounded by regions of more diffuse, spatially extended emission. The 2D knots visible in Fig. 4 are clearly traced into the third dimension along the velocity axis. These clump-like regions have linewidths ranging from  $\sim 5$  to  $\sim 17 \text{ km s}^{-1}$ . The two brightest, broadest velocity features are found in proximity to the H II regions IRAS 16164–5046 ( $\sim 16:20:15$ ,  $-50:53$ ; see the centre pv-array at offset  $\sim -5$  arcmin) and G333.6–0.2 ( $\sim 16:22:15$ ,  $-50:06$ ; see the bottom pv-array at offset  $\sim 27$  arcmin) whose linewidths are  $\sim 12$  and  $\sim 17 \text{ km s}^{-1}$ , respectively.

A large-scale velocity gradient across the GMC complex is apparent in the pv-arrays in Fig. 8, extending from an angular offset of  $\sim -25$  to 40 arcmin, and its direction is along/parallel to the main axis of emission in the GMC. At offsets below  $-25$  arcmin, the gradient changes direction and steepens, such that at either spatial extreme the ‘ends’ of the GMC are only separated in velocity by a few  $\text{km s}^{-1}$ .

The relatively linear change in velocity of  $\sim 10 \text{ km s}^{-1}$  over  $\sim 65$  arcmin corresponds to a gradient of  $0.2 \text{ km s}^{-1} \text{ arcmin}^{-1}$ . We do not consider this to be due to Galactic rotation, which gives a gradient of  $\sim 0.04 \text{ km s}^{-1} \text{ pc}^{-1}$  for an angular separation of  $\sim 65$  arcmin at  $b = 333^\circ$ . On one hand, if our measured velocity differential is due to Galactic rotation, the length of the GMC that this is measured over would correspond to  $\sim 250 \text{ pc}$ . At a distance of 3.6 kpc, 65 arcmin

would then correspond to a projected length of  $\sim 70 \text{ pc}$ . Therefore, we would have to be viewing an extended GMC at a large aspect ratio, nearly end-on, which seems unlikely. On the other hand, if we are viewing the GMC face-on such that our line of sight is perpendicular to its long axis and therefore 70 pc is actually the full length of this region, then our measured gradient corresponds to  $0.2 \text{ km s}^{-1} \text{ pc}^{-1}$ . This exceeds by a factor of 5 the value expected for Galactic rotation.

#### 4 CLUMP ANALYSIS

In order to study the structure of the emission in the GMC, we have used the CLUMPFIND algorithm of Williams et al. (1994) to decompose it into clumps. CLUMPFIND is an automated routine which searches through the data at user-specified brightness levels and assigns the emission found enclosed by these levels to discrete clumps. The algorithm reports the properties of the clump fits, viz: centre position, peak pixel value in the clump, the sum of the pixel values in the clump, clump radius and the number of pixels contained in the clump. In this fashion, physical clump sizes, densities and masses can be measured if the distance is known and assumptions of optically thin, thermalized emission are invoked where necessary. It is then possible to use the fits to investigate such things as the scaling relationship between mass and radius, and the mass spectrum of the clumps.

In this paper, we wish to compare the structure of the  $^{13}\text{CO}$  emission with that of the dust revealed in the SEST and *MSX* data.

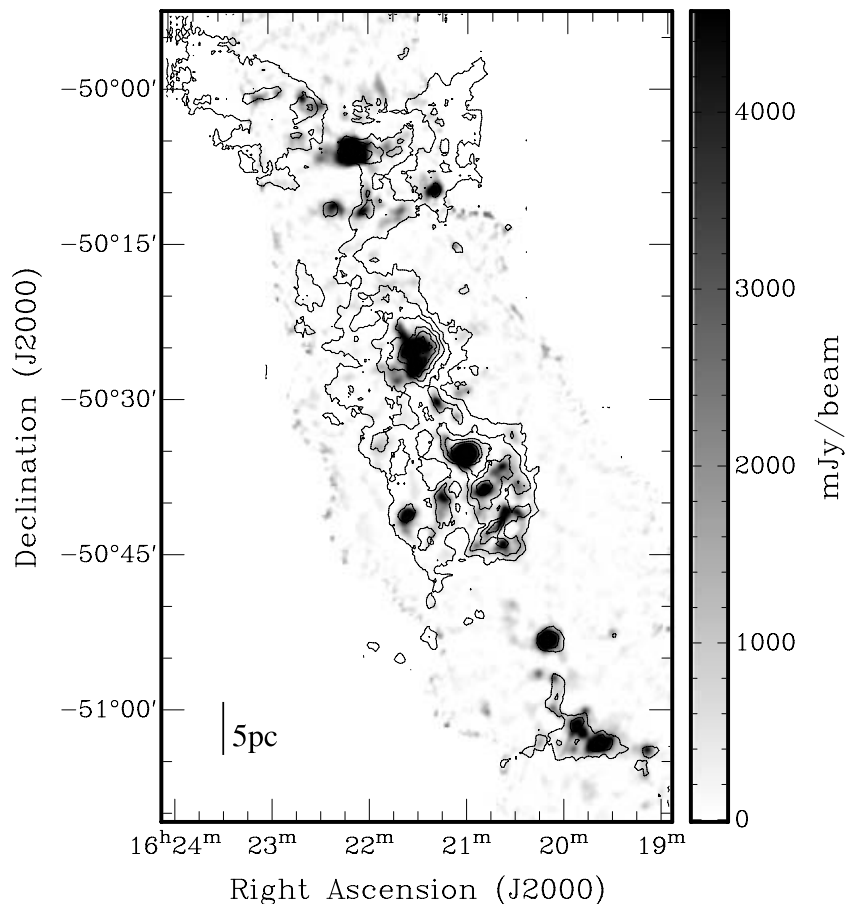


**Figure 7.** Grey-scale plot of the 1.2-mm SEST dust continuum image that has been regridded to the Mopra  $^{13}\text{CO}$  cell spacing and smoothed to the same resolution, overlaid with contours of the integrated  $^{13}\text{CO}$  emission from the GMC, starting from 30 per cent of the peak and incrementing in steps of 10 per cent (as in Fig. 4). The scale bar indicates the displayed stretch in brightness of the 1.2-mm image; the actual peak is  $52 \text{ Jy beam}^{-1}$ .

Therefore, we present the CLUMPFIND analysis we have conducted on the total intensity (zeroth moment)  $^{13}\text{CO}$  gas data as this is most suitable for comparison with the 2D dust data. The CLUMPFIND fits were made to the 2D gas data integrated over the velocity range of the GMC only, from  $-65$  to  $-35 \text{ km s}^{-1}$ . We have also decomposed the emission in the convolved-down mm-dust and mid-IR images using CLUMPFIND in order to compare the clumps found at various wavelengths.

Williams et al. (1994) detail how CLUMPFIND works best when applied to the data with a base contour level of the  $2\sigma$  rms noise level and with succeeding steps that increment by this level. The measured  $2\sigma$  rms off-source noise level in the convolved-down images was  $50 \text{ mJy beam}^{-1}$  (mm-dust) and  $2 \times 10^{-6} \text{ W m}^{-2} \text{ sr}^{-1}$  (mid-IR). Although the latter was indeed the step size used in the analysis of the mid-IR data, we actually set threshold level in this case to be  $4\sigma$  as the  $2\sigma$  level emission proved to be highly extended.

The low-level total intensity emission in the  $^{13}\text{CO}$  data is also smooth and extended (Fig. 4) with many filamentary features. To facilitate the clump fitting in these data, we found that clipping each channel at  $16\sigma$  rms level of  $2.9 \text{ K channel}^{-1}$  before making a zeroth moment image eliminated the emission contributed by the extended, filamentary, non-clump-like structures. We then applied the clump fitting routine to the clipped image using nine contours with a start and increment level of  $9 \text{ K km s}^{-1}$ . The structure enclosed by the base contour level is indicated in Fig. 9. We then applied the positions and sizes of the fits found in this way to a zeroth moment

image which had been constructed without any clipping in order to measure the peak and summed data values from the unclipped data. Note that the  $1\sigma$  rms level of the unclipped zeroth moment image is  $5 \text{ K km s}^{-1}$  ( $T_A^*$ ).

We found 61  $^{13}\text{CO}$  clumps, and in Table 1 we detail their properties; all have diameters greater than the Mopra beam size. The temperatures are in terms of main beam brightness temperature  $T_{\text{MB}}$ , given by  $T_{\text{MB}} = T_A^* / f\eta$ , where the filling factor  $f$  is assumed to be unity. The radius given by CLUMPFIND is that for a circle of equivalent area to that found in the clump fit. The radii in Table 1 are convolved with the beam and are calculated using a distance  $D = 3.6 \text{ kpc}$ . The clump column densities and masses were derived as described in Section 4.1.1. In Fig. 9, we show the positions of the  $^{13}\text{CO}$  clump fits overlaid on a grey-scale zeroth moment image of the  $^{13}\text{CO}$  GMC emission. The fits are represented by circles of size proportional to the local thermodynamic equilibrium (LTE) mass calculated using the fit (see Section 4.1). The centre positions of the seven brightest clumps are within  $\sim 3$  arcmin of known H II regions listed in the SIMBAD data base (see also Bik et al. 2005). From clumps 1–7, these are, respectively, IRAS 16172–5028, IRAS 16172–5018, IRAS 16172–5018, G333.0–0.4, G333.6–0.2, G333.0–0.4 and IRAS 16164–5046 (see Fig. 3). We will discuss the  $^{13}\text{CO}$  associations of the H II regions in a subsequent publication.

From performing CLUMPFIND on the mm-dust and mid-IR data within the region defined by the  $^{13}\text{CO}$  Mopra observations, we found 105 believable clumps in the mm-dust data and 98 in the mid-IR.

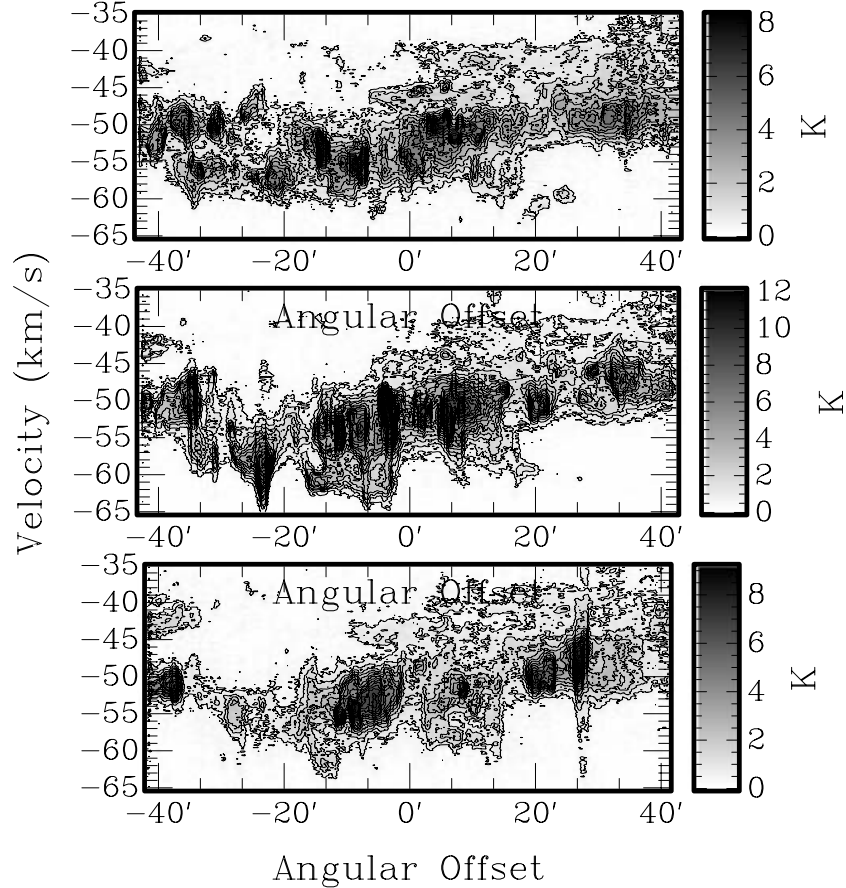


**Figure 8.** Position–velocity slices taken along/parallel to the main axis of emission as illustrated in Fig. 4 over the velocity range attributed to the GMC only ( $-65$  to  $-35$   $\text{km s}^{-1}$ ). The top plot shows the easternmost cut and the bottom plot the westernmost. The offsets are with respect to the slice central positions: top 16:21:32,  $-50:31:40$ ; middle 16:21:09,  $-50:31:55$  and bottom 16:20:49,  $-50:30:25$ . The PA of the slices is  $\sim 25^\circ$  E of N. Positive angular offsets correspond to more northerly positions. Contours are plotted at increments of the  $3\sigma$  rms noise level per channel of  $0.55$   $\text{K km s}^{-1}$ .

The mm-dust image contains artefacts at the field edges and has a slightly different field of view; we were careful to discard any erroneous/outlying fits, which were 34 in number. We also applied brightness level and size criteria such that the peaks of believable clumps were in excess of the  $3\sigma$  level and the diameters were greater than the beam size. Note that applying a  $5\sigma$  level cut-off to the 1.2-mm data reduced the number of believable clumps to 97. This is consistent with the number found by Mookerjee et al. (2004), who detail finding 95 clumps from applying CLUMPFIND to their full-resolution data, with a  $5\sigma$  cut-off level applied. The derived properties of the fits to the 1.2-mm dust data are discussed further in Section 4.1.6

We correlated the centre positions of the  $^{13}\text{CO}$  clump fits with those of the clumps found in the mm-dust and mid-IR data. Within one beam size (33 arcsec), 32/61  $^{13}\text{CO}$  clump fits are associated with either a mid-IR or a mm-dust clump fit, and the remaining 29  $^{13}\text{CO}$  clump fits have no associations in the other data sets. Of the  $^{13}\text{CO}$  clump fits with associations within the beam size, 29 are associated with a mm-dust clump fit, 12 with a mid-IR clump fit, and nine  $^{13}\text{CO}$  clump fits have both mid-IR and mm-dust associations. The properties of the associated clumps are grouped in Table 2. The masses were derived as detailed in Section 4.1. In Fig. 10, we plot the correlations of the masses and radii of the 29  $^{13}\text{CO}$  and mm-dust clumps found with centre positions within a beam size of each other.

The clump properties are not strongly correlated, which suggests that the gas and dust clumps paired in this way are themselves not strongly correlated and that they are tracing different components of the GMC. To quantify this, least-squares fits to the scatter plots give the correlations  $M_{^{13}\text{CO}} \propto M_{\text{mm}}^{0.44 \pm 0.10}$  and  $R_{^{13}\text{CO}} \propto R_{\text{mm}}^{0.74 \pm 0.22}$ .

If instead of considering the centre positions of the dust and gas clumps, we consider whether the clumps overlap, we find that 56/61  $^{13}\text{CO}$  clumps overlap with a 1.2-mm clump. Of the five not associated, four are partly or fully outside the SEST field, so effectively all of the  $^{13}\text{CO}$  clumps overlap with a 1.2-mm clump. Therefore, although the gas and dust appear to trace different components of the GMC, they may not be entirely unrelated. However, we are taking the more conservative approach of identifying associated gas and dust clumps according to their centre positions, as outlined previously.

## 4.1 Clump properties

### 4.1.1 $^{13}\text{CO}$ clump masses

We obtained clump column densities  $N(^{13}\text{CO})$  and total LTE masses from the  $^{13}\text{CO}$  data by using the analysis method of Bourke et al. (1997) and approximating it to the optically thin case

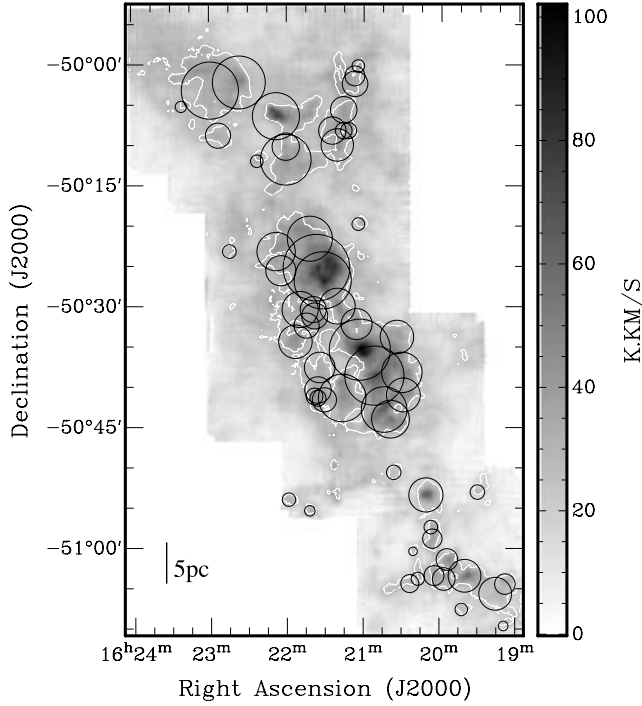


**Figure 9.** Grey-scale of the integrated  $^{13}\text{CO}$  emission (as Fig. 4) from the GMC only, overlaid with the 61 CLUMPFIND gas clump fits, with symbol size proportional to the mass calculated from the fit (Section 4.1). The white contour delineates the structure enclosed by the  $9 \text{ K km s}^{-1}$  level of the moment image that was constructed with a  $16\sigma$  per channel clip level and used to find the clump fits (Section 4).

( $\tau_{^{13}\text{CO}} \ll 1$ ),  $T_{\text{ex}} \int \tau_{^{13}\text{CO}}(v) dv \sim \int T_{\text{MB}}(v) dv$  such that

$$N(^{13}\text{CO}) = \frac{2.42 \times 10^{14}}{1 - \exp(-5.29/T_{\text{ex}})} \int T_{\text{MB}} dv \quad (1)$$

with the excitation and main beam brightness temperatures (respectively  $T_{\text{ex}}$  and  $T_{\text{MB}}$ ) in K and velocity  $v$  in  $\text{km s}^{-1}$ . Optical depth effects are assumed to be minimal, and we discuss this further in Section 4.1.3. If thermalized lines are assumed, then the kinetic temperature  $T_{\text{kin}}$  is approximately the excitation temperature  $T_{\text{ex}}$ . We then make the further assumption that the different isotopes have the same  $T_{\text{kin}}$ , and therefore the same  $T_{\text{ex}}$ , and that they are emitted from the same volume. In this case, we can take  $T_{\text{ex}}(^{13}\text{CO}) \sim T_{\text{ex}}(^{12}\text{CO}) = 20 \text{ K}$ , which we obtained from the peak  $T_{\text{MB}}$  measured from the optically thick  $^{12}\text{CO}$  lines observed by Mookerjee et al. (2005) from selected clumps in the GMC, and by assuming that the  $^{12}\text{CO}$  emission completely fills the beam. For  $\int T_{\text{MB}} dv$ , we used the average pixel value measured in the clump.

Once again following the method of Bourke et al. (1997) in the optically thin limit, the total LTE mass measured from the molecular gas is given by

$$\frac{M_{^{13}\text{CO}}}{M_{\odot}} = \frac{\mu_{\text{m}}}{2.72 m_{\text{H}}} \frac{[\text{H}_2/^{13}\text{CO}]}{7 \times 10^5} \left( \frac{D}{\text{kpc}} \right)^2 \times \frac{0.312}{1 - \exp(-5.29/T_{\text{ex}})} \int \int T_{\text{MB}} dv d\Omega \quad (2)$$

where we have taken a  $[\text{H}_2/^{13}\text{CO}]$  abundance ratio of  $7 \times 10^5$  (Frerking, Langer & Wilson 1982; Bourke et al. 1997), a mean molecular weight of  $\mu_{\text{M}} = 1.36 m_{\text{H}}$  (where  $m_{\text{H}}$  is the mass of H)

to account for the presence of He, the distance  $D = 3.6 \text{ kpc}$  and the clump area  $\Omega = \pi R_{^{13}\text{CO}}^2$ , where  $R_{^{13}\text{CO}}$  is the  $^{13}\text{CO}$  clump radius, is in  $\text{arcmin}^2$ . The masses and column densities derived from the  $^{13}\text{CO}$  clumps are given in Table 1. The total molecular LTE mass measured from the 61  $^{13}\text{CO}$  clumps is  $2.7 \times 10^5 M_{\odot}$ . By considering the total flux density in the unclipped moment image that the clump fits were made to, the total gas mass in the GMC is  $7.8 \times 10^5 M_{\odot}$ . Therefore, the gas clumps we have measured in the GMC are representative of slightly over a third of the available gas mass.

#### 4.1.2 $^{13}\text{CO}$ clump mass–radius scaling law and mass spectrum

Molecular clouds possess clumpy structure that appears self-similar, or fractal, on all scales. A manifestation of this is that when decomposition algorithms are applied to GMC data to identify the clumps, the hierarchical scaling behaviour of their derived properties is replicated from cloud to cloud. Larson (1981) showed empirically that for molecular clouds of size  $\sim 1\text{--}1000 \text{ pc}$ , constituent clumps possess properties viz mass, density and linewidth that scale with radius, such as  $M \propto R^2$  and  $\Delta v \propto R^{0.5}$ . This latter condition arises naturally when considering gravitationally bound clumps in virial equilibrium, but the same scaling relations are nevertheless also found in clouds containing clumps well below virial equilibrium (Kramer et al. 1998). (Mac Low & Klessen 2004, and references therein) argue that the size–linewidth relation is not due to virial conditions, but rather due to a supersonic turbulent cascade. Indeed, the apparent universality of the scaling relations suggests the presence of a mechanism capable of producing correlations over all scales while being invariant to the specifics of local conditions, such as turbulence.

The hierarchical nature of cloud structure is also seen in their composite clump mass spectra, given by  $dN/dM \propto M^{-\alpha_{\text{M}}}$ . Molecular line tracers produce  $\alpha_{\text{M}}$  in the range  $\sim 1.4\text{--}1.9$  (e.g. Heithausen et al. 1998; Simon et al. 2001, and references therein). In comparison, observations of dust cores, give  $\alpha_{\text{M}}$  from  $1.9\text{--}2.5$  (Mac Low & Klessen 2004, and references therein), which is closer to the stellar initial mass function (IMF) (Scalo 1986). The difference between clump and core mass spectra can be attributed to cores being in general bounded, whilst clump distributions contain large fragments which are unbounded. Simon et al. (2001) note that discrepancies between the mass spectra obtained from molecules and those from dust can also arise due to incorrect assumptions in the mass derivations and essentially the different components traced by molecules and dust in molecular clouds. Kramer et al. (1998) give an in-depth discussion on the possible reasons for the differences between the clump mass spectral index and the steeper stellar IMF based on the processes that occur when a clump crosses the threshold to become a star.

In Fig. 11, we plot the mass–radius scatter plot for the 61 fitted  $^{13}\text{CO}$  clumps. A least-squares fit to the plot gives a strong correlation (with coefficient 0.99) of  $M_{^{13}\text{CO}} \propto R_{^{13}\text{CO}}^{2.27 \pm 0.04}$ , which is consistent with the Larson (1981) scaling law and suggests that the column density in the clumps is close to being constant. This can be seen in Table 1, and is shown graphically by the top right plot in Fig. 11 where  $N_{^{13}\text{CO}} \propto M_{^{13}\text{CO}}^{0.14 \pm 0.02}$ . Our mass–radius relationship for this GMC is also consistent with those found in the four molecular cloud complexes surveyed in the Galactic Ring project of Simon et al. (2001). The histogram of the fitted clump radii shows no strong peak in the distribution, with radii ranging from  $\sim 0.5$  to  $3 \text{ pc}$ . We also show the histogram of the binned  $^{13}\text{CO}$  clump masses, with Poisson error bars. The LTE gas masses span 2 orders of magnitude, from

**Table 1.** Properties of the 61  $^{13}\text{CO}$  clumps found by CLUMPFIND. The columns are as follows. (1)  $^{13}\text{CO}$  clump number; (2) and (3) position of fit; (4) peak  $^{13}\text{CO}$  brightness; (5)  $^{13}\text{CO}$  brightness summed over all pixels in clump; (6) clump radius (convolved with the beam and for  $D = 3.6$  kpc); (7)  $^{13}\text{CO}$  column density; (8) total LTE molecular mass calculated from the  $^{13}\text{CO}$  data; (9) associated mm-dust SEST (S) or mid-IR *MSX* (M) clump fit with a centre position within a beam size of that of the  $^{13}\text{CO}$  clump fit (see Table 2 for more details of the associated fits).

$N_{^{13}\text{CO}}$	RA	Dec.	Peak	Sum	$R_{^{13}\text{CO}}$	$N(^{13}\text{CO})$	$M_{^{13}\text{CO}}$	mm-dust
(1)	(h m s)	(d m s)	( $10\text{ K km s}^{-1}$ )	( $10^3\text{ K km s}^{-1}$ )	(pc)	( $10^{16}\text{ cm}^{-2}$ )	( $10^3 M_{\odot}$ )	or mid-IR?
(1)	(2)	(3)	(4)	(5)	(6)	(7)	(8)	
1	16 21 03	-50 35 27	18.5	46.0	2.6	10.1	16.0	S,M
2	16 21 32	-50 26 51	15.8	41.4	2.4	10.3	14.4	S
3	16 21 37	-50 25 15	15.3	54.2	2.8	10.1	18.9	-
4	16 20 52	-50 38 39	13.3	44.1	2.6	9.3	15.4	S,M
5	16 22 08	-50 06 27	13.8	27.4	2.2	7.9	9.5	S
6	16 20 44	-50 42 51	11.8	25.5	2.1	8.0	8.9	-
7	16 20 11	-50 53 27	12.0	14.4	1.8	6.2	5.0	S,M
8	16 20 39	-50 44 03	10.3	17.4	1.9	7.1	6.1	S,M
9	16 19 40	-51 03 27	10.5	13.3	1.7	6.6	4.6	S,M
10	16 20 30	-50 38 15	9.3	20.2	2.0	7.5	7.0	S
11	16 21 17	-50 41 27	8.8	27.9	2.5	6.5	9.7	S
12	16 22 01	-50 11 51	8.5	31.3	2.7	6.4	10.9	-
13	16 22 37	-50 02 15	9.2	35.3	2.7	6.8	12.3	-
14	16 21 21	-50 30 03	8.8	15.7	1.8	6.9	5.5	S,M
15	16 19 54	-51 01 27	8.9	5.8	1.1	6.9	2.0	S
16	16 20 29	-50 41 03	8.5	14.0	1.7	6.7	4.9	S
17	16 21 53	-50 34 27	8.4	13.7	1.8	6.4	4.8	S
18	16 21 38	-50 31 15	8.3	8.4	1.3	7.0	2.9	-
19	16 21 38	-50 41 15	8.1	3.5	0.9	7.0	1.2	S,M
20	16 21 36	-50 40 27	7.3	8.8	1.5	6.0	3.0	-
21	16 21 39	-50 30 27	8.1	8.3	1.3	7.1	2.9	M
22	16 21 42	-50 21 39	8.9	25.0	2.2	7.6	8.7	M
23	16 21 31	-50 41 39	6.8	7.2	1.3	5.8	2.5	-
24	16 21 36	-50 41 27	8.0	3.2	0.8	6.9	1.1	S
25	16 22 01	-50 10 15	7.2	9.3	1.5	6.0	3.2	S
26	16 20 34	-50 33 51	7.8	13.8	1.8	6.4	4.8	S
27	16 21 45	-50 32 27	7.9	7.8	1.3	6.9	2.7	-
28	16 21 16	-50 05 39	7.3	8.5	1.4	6.4	3.0	-
29	16 21 21	-50 10 03	8.0	12.9	1.8	6.0	4.5	S,M
30	16 20 06	-50 58 51	7.0	4.7	1.1	6.0	1.6	S
31	16 20 04	-51 03 27	7.3	4.7	1.1	6.2	1.7	S
32	16 19 08	-51 04 27	6.2	5.2	1.2	5.1	1.8	S,M
33	16 21 50	-50 30 27	7.5	16.0	2.0	6.0	5.6	-
34	16 21 06	-50 32 15	8.4	11.9	1.6	6.6	4.1	S
35	16 22 08	-50 23 15	8.2	18.2	2.0	7.0	6.3	-
36	16 19 30	-50 53 03	5.2	2.6	1.0	4.0	0.9	S
37	16 21 16	-50 08 15	7.6	3.4	0.8	6.9	1.2	-
38	16 21 59	-50 54 03	5.6	2.2	0.8	4.9	0.8	-
39	16 21 24	-50 08 15	7.1	9.3	1.5	6.3	3.2	-
40	16 21 34	-50 37 39	6.3	11.5	1.7	5.6	4.0	-
41	16 21 07	-50 02 27	7.3	8.0	1.3	6.6	2.8	-
42	16 21 07	-50 01 27	7.1	5.0	1.1	6.5	1.7	M
43	16 22 05	-50 25 39	7.2	11.2	1.6	6.3	3.9	-
44	16 21 42	-50 55 27	6.1	1.4	0.6	5.3	0.5	-
45	16 20 07	-50 57 27	6.5	2.3	0.8	5.6	0.8	S
46	16 22 59	-50 03 15	7.1	41.3	3.1	6.1	14.4	-
47	16 19 16	-51 05 39	5.9	13.2	2.0	4.7	4.6	-
48	16 20 23	-51 04 27	5.7	3.9	1.1	4.9	1.4	-
49	16 19 57	-51 03 51	7.1	6.2	1.2	5.9	2.2	S
50	16 21 12	-50 08 15	7.2	3.1	0.8	6.6	1.1	-
51	16 21 05	-50 00 15	6.4	1.9	0.7	5.8	0.7	-
52	16 19 42	-51 07 39	4.9	1.9	0.8	4.3	0.7	-
53	16 22 53	-50 08 51	6.3	7.7	1.4	5.5	2.7	-
54	16 21 04	-50 19 51	5.9	2.0	0.7	5.3	0.7	S
55	16 20 36	-50 50 39	5.0	2.6	0.9	4.5	0.9	-
56	16 22 23	-50 12 03	6.2	1.9	0.7	5.5	0.7	-
57	16 20 21	-51 00 27	4.9	0.9	0.5	4.4	0.3	S
58	16 20 17	-51 03 51	6.0	2.1	0.8	5.3	0.7	S
59	16 23 22	-50 05 15	6.1	1.5	0.6	5.7	0.5	-
60	16 19 09	-51 09 39	4.8	1.1	0.6	4.4	0.4	S
61	16 22 45	-50 23 15	5.7	2.3	0.8	5.0	0.8	-

**Table 2.** Properties of associated mm-dust (SEST) and mid-IR (*MSX*) clump fits with centre positions within a beam size of that of a  $^{13}\text{CO}$  clump. The columns are as follows. (1) Associated  $^{13}\text{CO}$  clump number from Table 1; (2) 1.2-mm clump number (see Table 3 for more details); (3) angular offset of centre positions of associated  $^{13}\text{CO}$  and mm-dust clumps; (4) peak flux density per beam area in mm-dust clump; (5) gas:mm-dust mass ratio for relevant paired clumps (masses are derived as detailed in Section 4.1); Columns (6) and (7) are Columns (3) and (4) but for the associated mid-IR clump fits; (8) radius of mid-IR fit.

$N_{^{13}\text{CO}}$	$N_{\text{mm}}$	mm clumps			21- $\mu\text{m}$ clumps		$R_{\text{mir}}$ (pc)
		Offset (arcsec)	Peak ( $\text{Jy beam}^{-1}$ )	$M_{^{13}\text{CO}} : M_{\text{mm}}$	Offset (arcsec)	Peak ( $10^{-5} \text{ W m}^{-2} \text{ sr}^{-1}$ )	
(1)	(2)	(3)	(4)	(5)	(6)	(7)	(8)
1	3	12	13.4	0.7	1	62.8	2.6
2	4	27	9.3	1.3	–	–	–
4	7	17	4.5	2.7	15	8.3	1.8
5	1	27	52.1	0.2	–	–	–
7	2	12	16.1	0.3	28	71.5	2.0
8	16	12	1.4	2.6	12	7.9	1.7
9	8	17	4.2	0.5	13	10.6	1.8
10	30	12	0.7	4.7	–	–	–
11	45	12	0.5	10.8	–	–	–
14	14	27	1.5	3.3	25	3.1	1.3
15	10	27	2.7	0.6	–	–	–
16	22	12	1.1	3.2	–	–	–
17	66	27	0.4	6.3	–	–	–
19	9	12	3.7	0.2	23	0.8	3.4
21	–	–	–	–	18	3.1	2.3
22	–	–	–	–	25	0.8	1.7
24	9	17	3.7	0.2	–	–	–
25	28	12	0.7	3.8	–	–	–
26	74	17	0.3	11.4	–	–	–
29	5	12	5.5	0.8	12	3.0	1.6
30	90	17	0.2	5.1	–	–	–
31	85	12	0.3	5.9	–	–	–
32	21	27	1.1	0.9	26	2.2	1.3
34	55	27	0.4	11.6	–	–	–
36	52	17	0.4	2.4	–	–	–
42	–	–	–	–	27	0.8	1.5
45	24	12	0.8	1.0	–	–	–
49	33	17	0.6	1.8	–	–	–
54	121	27	0.1	5.7	–	–	–
57	117	27	0.1	1.5	–	–	–
58	64	27	0.4	1.3	–	–	–
60	81	17	0.3	2.5	–	–	–

Note that masses cannot be determined from the optically thick 21- $\mu\text{m}$  data.

$\sim 300 M_{\odot}$  to  $1.9 \times 10^4 M_{\odot}$ . With these radii and masses, the clumps we have detected are larger in scale than individual star-forming cores.

Following a similar analysis to that described in Simon et al. (2001), the completeness limit to the masses is dependent on both the rms level of the data and the threshold contour level used to define the structure to be fitted by CLUMPFIND. The minimum pixel value in the unclipped moment image that lies within this base contour level (Fig. 9) is  $41 \text{ K km s}^{-1}$  ( $T_{\text{A}}^*$ ). Using equation (2) with a minimum clump size given by the beam size, we find that CLUMPFIND was sensitive to a minimum mass  $M_{\text{min}} \sim 155 M_{\odot}$ . The  $1\sigma$  rms level of the image is  $5 \text{ K km s}^{-1}$  ( $T_{\text{A}}^*$ ). Again using the limiting clump size to be the beam size, the  $10\sigma$  mass  $M_{10\sigma} \sim 200 M_{\odot}$ . The completeness limit, to a  $10\sigma$  confidence level, is then  $M_{\text{c}} = M_{\text{min}} + M_{10\sigma} = 355 M_{\odot}$ . This is indicated by the dashed line in Fig. 11. The low-mass end of the spectrum will be undersampled because we precluded the detection of smaller, low-brightness clumps by setting a high clip level to facilitate the fitting of the clumps in the

first place. However, a fit to the mass spectrum is dominated by the high mass end of the distribution so this undersampling in itself should not affect such a fit.

We have made a linear least-squares fit to the mass distribution above the turnover in order to measure the mass spectral index  $\alpha_{\text{M}}$ . Fitting to the  $^{13}\text{CO}$  mass distribution above the turnover gives  $\alpha_{\text{M}} = 2.22 \pm 0.41$ . This is a poor fit which is not well constrained nor robust when subjected to variations in the binning: varying the bin size by  $\sim \pm 10$  per cent and fitting to the bins above the resulting turnovers produce a variation in  $\alpha_{\text{M}}$  of up to 20 per cent. The plot serves to illustrate the non-clump-like structure of the gas and is a manifestation of the relatively low relative brightness contrast in the gas data. This lack of clumpiness in the gas is also illustrated by the relatively few  $^{13}\text{CO}$  clump fits when compared with the number found in the mid-IR and mm-dust data. The dust is tracing dense, clump-like condensations whereas the gas is more extended, as Figs 6 and 7 bear witness to, and the gas and dust structures have no strong correlation.

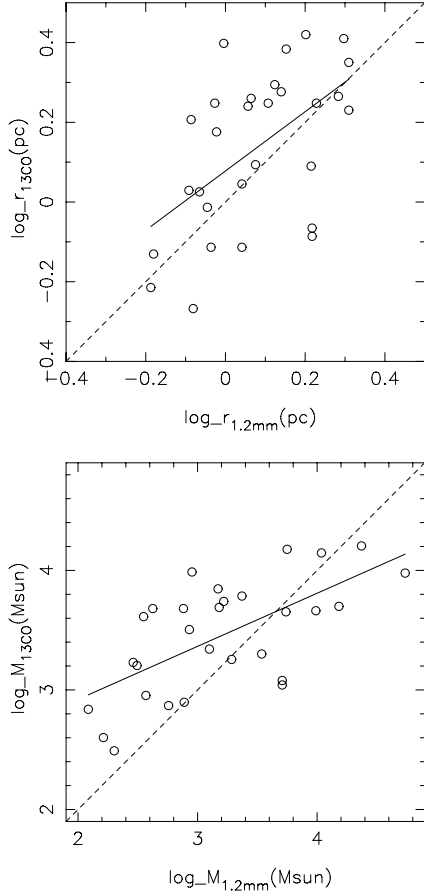


**Figure 10.** Scatter plots of (top) radii and (bottom) masses for the 29  $^{13}\text{CO}$ -mm-dust clump pairings found with centre positions within one beam size of each other. The least-squares fits of  $R_{^{13}\text{CO}} \propto R_{\text{mm}}^{0.74 \pm 0.22}$  and  $M_{^{13}\text{CO}} \propto M_{\text{mm}}^{0.44 \pm 0.10}$  are shown, and the dashed lines denote  $R_{^{13}\text{CO}} = R_{\text{mm}}$  and  $M_{^{13}\text{CO}} = M_{\text{mm}}$ , respectively.

#### 4.1.3 A note on optical depth effects

At large column densities,  $^{13}\text{CO}$  is prone to optical depth effects, which if present, will cause the mass in a clump to be underestimated. Whether this occurs can be assessed by comparing the  $^{13}\text{CO}$  line profile to that of the rarer  $\text{C}^{18}\text{O}$  isotopomer, for which the abundance ratio  $^{13}\text{CO}/\text{C}^{18}\text{O}$  is taken as 5.5 based on solar abundances of carbon. Mookerjee et al. (2005) took pointed observations in  $\text{C}^{18}\text{O}$  of some of the bright knots in the G333 region, and we compared these profiles with those taken in  $^{13}\text{CO}$  at the same position; examples are shown in Fig. 12.

In a few of the brightest knots, the  $^{13}\text{CO}:\text{C}^{18}\text{O}$  ratio at the line peaks is around 3 or 4, giving a maximum error in the masses of the brightest clumps that is a factor of 2. However, we stress that the optical depth effects were only seen in the few brightest knots and then only at the peaks of the lines; the integrated intensities of the species at each position were also measured and these gave ratios of around 5:1, as expected for optically thin emission. It is the integrated intensity that is used to calculate the column densities and masses, hence we consider the effect of  $^{13}\text{CO}$  optical depth on the clump mass calculations to be small in all but the brightest clumps. We are in the process of mapping the region in  $\text{C}^{18}\text{O}$  to further investigate optical depth effects in the GMC, and to determine whether this assumption is indeed true.

#### 4.1.4 1.2-mm dust clump masses

To determine the total masses  $M_{\text{mm}}$  of the clumps fitted to the mm-dust emission, we followed the analysis of Mookerjee et al. (2004) and, assuming that the 1.2-mm emission is optically thin, we used

$$M_{\text{mm}} = \frac{F_{\nu} D^2}{\kappa_{\nu} B_{\nu}(T_{\text{mm}})}, \quad (3)$$

where  $B_{\nu}(T_{\text{mm}})$  is the Planck function at the dust temperature  $T_{\text{mm}}$ . We adopted  $T_{\text{mm}} = 20$  K, as used in the analysis of Mookerjee et al. (2004)<sup>1</sup> and also by other authors (e.g. Hill et al. 2005, and references therein). The dust mass opacity coefficient was obtained using  $\kappa_{\nu} = \kappa_{230\text{GHz}}(\nu/230\text{GHz})^{\beta}$  with  $\kappa_{230\text{GHz}} = 0.005\text{ g}^{-1}\text{ cm}^2$  and dust emissivity index  $\beta = 2$  (as in Mookerjee et al. 2004). This assumes a gas:dust mass ratio of 100. The properties of the mm-dust clump fits are given in Table 3 and are detailed further in the succeeding sections.

#### 4.1.5 1.2-mm clump mass–radius scaling law and mass spectrum

In Fig. 13, we show the mass–radius scatter plot for the 105 clump fits to the convolved-down 1.2-mm data, with the least-squares fit  $M_{\text{mm}} \propto R_{\text{mm}}^{3.96 \pm 0.14}$  shown. The radii of the clump fits to the dust data span a smaller range than those to the  $^{13}\text{CO}$  shown in Fig. 11, with a distribution strongly peaked towards smaller clumps of radius  $\sim 1$  pc. The largest dust clumps have radii of  $\sim 2$  pc whereas the largest fitted gas clumps have radii of  $\sim 3$  pc, which again illustrates the relative compactness of the dust structures we are observing when compared with the gas. The dust clump radii we measure are slightly larger (by  $\sim$  a few per cent) than those measured by Mookerjee et al. (2004). This is because both studies are considering radii convolved with the beam, and here we have convolved down the dust data. Our dust clump integrated flux densities and hence masses are also slightly higher, again due to this difference in the beam size. For 11 of the more massive dust clumps, there is an added discrepancy between this work and that of Mookerjee et al. (2004) due to the aforementioned authors using  $T_{\text{mm}} = 40$  K for these regions whereas we used  $T_{\text{mm}} = 20$  K for all the clumps; see their paper for more details of the individual clumps affected. This leads to the relevant clumps having masses a factor of a few larger here than in Mookerjee et al. (2004), which is probably why the masses scale more steeply with radius (Fig. 13) in our analysis.

In Fig. 13, we also show a plot of the mass spectrum for the 1.2-mm dust clumps. The 105 mm-dust clump masses extend over three orders of magnitude whilst the 61  $^{13}\text{CO}$  clump masses only extend over two orders, although the lack of low mass gas clumps will in part be due to the clip level applied to the  $^{13}\text{CO}$  data before the fits could be made. Using equation (3) with a  $1\sigma$  level of  $50\text{ mJy beam}^{-1}$ , the minimum contour search level used in CLUMPFIND, and a 33-arcsec beam size, the limiting 1.2-mm clump mass detectable by CLUMPFIND is  $M_{\text{min}} \sim 20 M_{\odot}$ . From the rms noise level of  $25\text{ mJy beam}^{-1}$  and a clump size equal to the beam size, we find  $M_{10\sigma} = 95 M_{\odot}$ . Therefore, to a  $10\sigma$  confidence level, the completeness limit to the mm-dust masses is  $M_c \sim 115 M_{\odot}$  and this is indicated by the dashed line on the mass distribution plot; the spectrum turns over above this. A least-squares fit to the distribution above the turnover gives  $\alpha_M = 1.67 \pm 0.09$ . Varying the bin size by  $\sim \pm 10$  per cent results in a maximum change in  $\alpha_M$  of only 2 per cent. This index is

<sup>1</sup> Mookerjee et al. (2004) used 20 K in all their clumps apart from 11 which they associated with high mass star formation and for which they used 40 K. We use  $T_{\text{mm}} = 20$  K throughout.

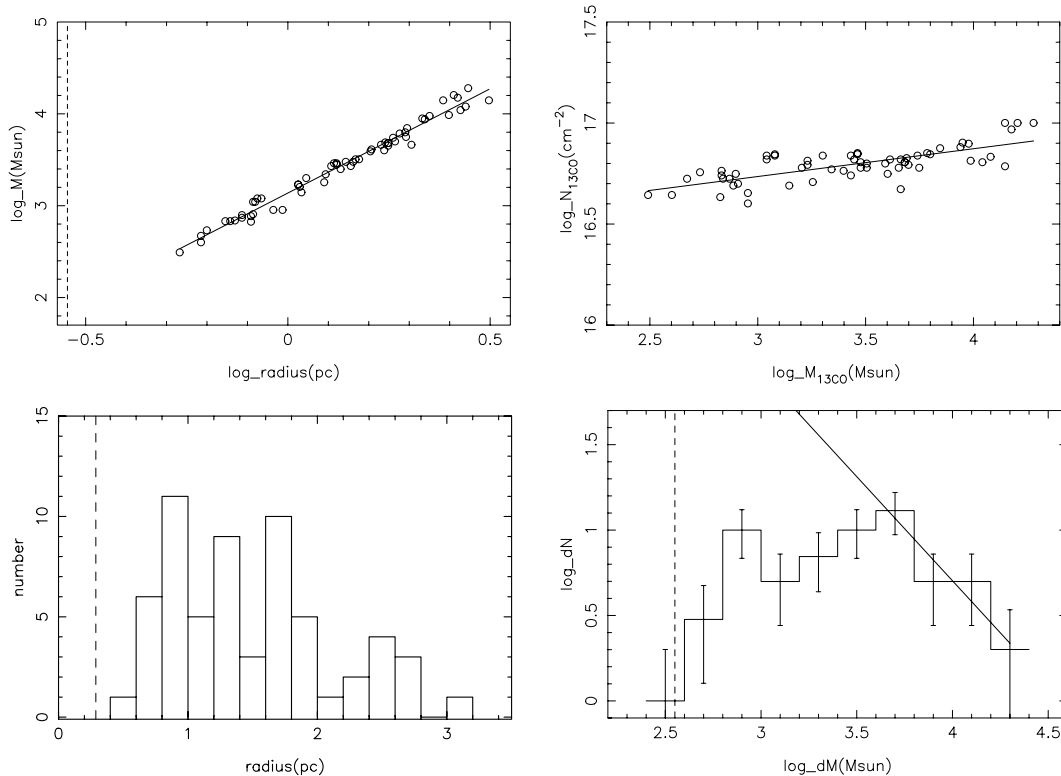


**Figure 11.** Plots of the parameters derived from the 61  $^{13}\text{CO}$  clump fits. Top left: mass–radius scatter plot, with a least-squares fit of  $M_{^{13}\text{CO}} \propto R_{^{13}\text{CO}}^{2.27 \pm 0.04}$ ; the limiting case of the beam radius at 3.6 kpc is indicated by the vertical dashed line. Top right: the variation of column density as a function of clump mass  $N_{^{13}\text{CO}} \propto M_{^{13}\text{CO}}^{0.14 \pm 0.02}$ . Bottom left: distribution of fitted clump radii; the limiting case of the beam radius at 3.6 kpc is indicated by the dotted line. Bottom right: mass spectrum with spectral index  $\alpha_M = 2.22 \pm 0.41$  fitted above the turnover. The  $355 M_{\odot}$  completeness limit is indicated by the dashed vertical line.

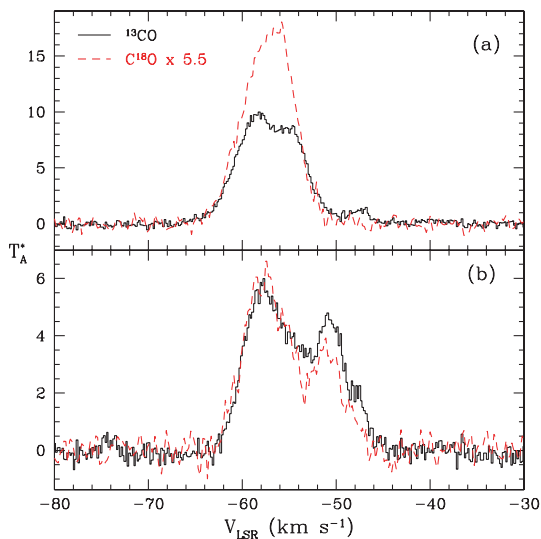


**Figure 12.** Mopra spectra of  $^{13}\text{CO}$  (this paper) and  $\text{C}^{18}\text{O}$  (Mookerjea et al. 2005), the latter scaled by the terrestrial abundance ratio of 5.5. The spectra are taken at two positions: (a) a bright mm clump at 16:20:12,  $-50:53:17$  and (b) a weaker source at 16:21:36,  $-50:41:11$ .

in agreement with those measured by Mookerjea et al. (2004) using the full-resolution 1.2-mm data and the analysis tools GAUSSCLUMPS ( $\alpha_M = 1.5$ ) and CLUMPFIND ( $\alpha_M = 1.7$ ). It also illustrates how, despite a 30 per cent decrease in resolution, the mass spectrum of the dust clumps remains self-similar. It is likely that the slightly steeper

CLUMPFIND spectrum measured by Mookerjea et al. (2004) is a result of the difference in the high mass end of the distribution that results from our use of  $T_{\text{mm}} = 20$  K for all clumps compared with their use of  $T_{\text{mm}} = 40$  K for 11 of the more massive clumps. The 1.2-mm index is comparable with that expected from low-density molecular tracers such as CO (see the discussion in Section 4.1.2) rather than that for the denser conditions traced by dust, possibly an effect of the SEST beam size which was insufficient to detect cores ( $\leq 0.1$  pc) and only sensitive to clumps (Mookerjea et al. 2004). However, it is interesting that the clump fits to the optically thin total column density tracer (1.2-mm dust) display a power-law spectrum, whilst those to the low-density tracer ( $^{13}\text{CO}$ ) do not. In this sense, the dust data are displaying more evidence of a hierarchical turbulent regime than the gas, and we anticipate that our future studies with high-density molecular tracers such as CS will display similar structure and scaling properties to those of the 1.2-mm dust seen here. The effect of using the integrated gas data cannot be discounted though, and the analysis of the  $^{13}\text{CO}$  mass spectrum from the 3D data set will be presented in a subsequent publication.

#### 4.1.6 $^{13}\text{CO}$ properties of the 1.2-mm dust clumps

The results presented in the previous sections illustrate how, based on solely comparing the independent clump fits to the mm-dust and  $^{13}\text{CO}$  data sets, the gas and dust data are not strongly correlated: based on their centre positions, only 50 per cent of the  $^{13}\text{CO}$  clump fits are associated with either a mid-IR or mm-dust clump fit, to within a beam size. To provide an alternative analysis on the

**Table 3.** Properties of the 105 mm-dust clumps found by CLUMPFIND and associated  $^{13}\text{CO}$  measurements taken from the corresponding regions on the unclipped  $^{13}\text{CO}$  GMC moment image (see text for more details). The columns are as follows. (1) mm-dust clump number; (2) & (3) position of mm-dust clump fit; (4) clump radius (convolved with the beam and for  $D = 3.6$  kpc); (5) total flux density in mm-dust clump; (6) mass of mm-dust clump; (7) peak brightness measured from the  $^{13}\text{CO}$  image in the region of the mm-dust clump fit; (8) summed brightness measured from the  $^{13}\text{CO}$  image over the same pixels as the corresponding mm-dust clump fit; (9) column density of  $^{13}\text{CO}$  in this region; (10) LTE mass measured from the  $^{13}\text{CO}$ ; (11) gas:dust mass ratio over the region of the mm-dust clump fit. Note that those mm-dust clumps omitted from the numbering sequence in Column (1) correspond to ‘bad’ fits; see text for more details.

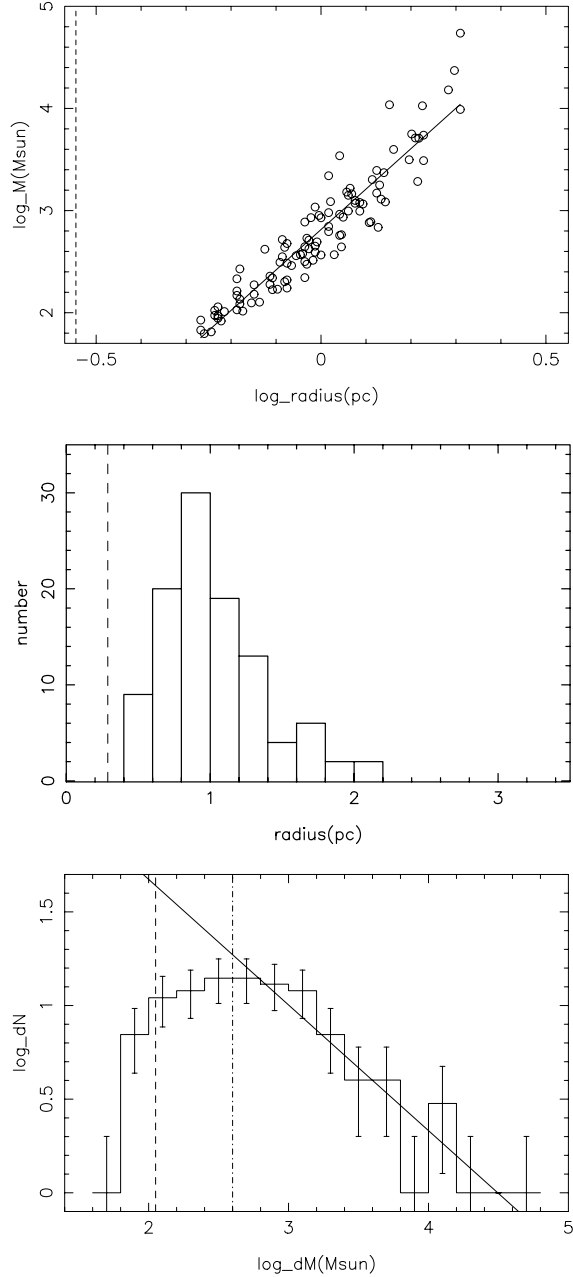
$N_{\text{mm}}$	mm-dust					$^{13}\text{CO}$				
	RA (h m s) (1)	Dec. (d m s) (3)	$R_{\text{mm}}$ (pc) (4)	$S_{\text{mm}}$ (Jy) (5)	$M_{\text{mm}}$ ( $10^3 M_{\odot}$ ) (6)	Peak ( $10 \text{ K km s}^{-1}$ ) (7)	Sum ( $10^3 \text{ K km s}^{-1}$ ) (8)	$N(^{13}\text{CO})$ ( $10^{16} \text{ cm}^{-2}$ ) (9)	$M_{^{13}\text{CO}}$ ( $10^3 M_{\odot}$ ) (10)	$M_{^{13}\text{CO}} : M_{\text{mm}}$ (11)
1	16 22 11	−50 06 15	2.0	145.2	54.5	13.8	20.4	7.2	7.1	0.1
2	16 20 12	−50 53 27	1.9	40.5	15.2	12.0	15.1	5.9	5.2	0.3
3	16 21 04	−50 35 27	2.0	62.6	23.5	18.5	31.2	11.6	10.9	0.5
4	16 21 33	−50 27 15	1.4	28.9	10.9	15.8	16.4	11.8	5.7	0.5
5	16 21 21	−50 09 51	1.7	14.6	5.5	8.0	12.6	6.4	4.4	0.8
6	16 21 33	−50 25 27	1.7	28.3	10.6	15.3	22.0	11.3	7.6	0.7
7	16 20 50	−50 38 51	1.6	15.0	5.6	13.3	17.4	10.1	6.1	1.1
8	16 19 39	−51 03 39	2.0	26.0	9.8	10.5	15.6	5.5	5.4	0.6
9	16 21 37	−50 41 15	1.7	13.6	5.1	8.1	12.5	6.7	4.3	0.8
10	16 19 53	−51 01 51	1.1	9.2	3.4	8.9	5.6	6.8	1.9	0.6
11	16 21 28	−50 25 03	1.6	13.7	5.1	15.3	22.2	12.4	7.7	1.5
12	16 20 38	−50 41 03	1.5	10.6	4.0	11.8	12.8	8.8	4.5	1.1
13	16 19 49	−51 02 27	1.0	5.9	2.2	7.2	4.1	5.5	1.4	0.6
14	16 21 19	−50 30 27	1.2	4.4	1.7	8.8	6.9	7.4	2.4	1.5
15	16 22 04	−50 12 03	1.3	5.4	2.0	8.5	7.4	6.4	2.6	1.3
16	16 20 39	−50 44 15	1.4	6.3	2.4	10.3	10.4	8.0	3.6	1.5
17	16 21 16	−50 39 39	1.3	6.6	2.5	8.8	8.3	6.9	2.9	1.2
18	16 22 22	−50 11 27	1.7	8.2	3.1	6.2	8.8	4.5	3.1	1.0
19	16 22 40	−50 01 03	1.2	3.9	1.5	8.7	6.6	6.9	2.3	1.6
20	16 20 39	−50 36 39	1.6	8.4	3.1	10.5	15.9	9.4	5.6	1.8
21	16 19 09	−51 04 03	1.6	5.1	1.9	6.2	8.0	4.3	2.8	1.5
22	16 20 30	−50 41 03	1.1	4.0	1.5	8.5	6.4	7.2	2.2	1.4
23	16 19 48	−51 00 27	1.2	3.2	1.2	6.6	3.1	3.0	1.1	0.9
24	16 20 07	−50 57 15	0.9	2.1	0.8	6.5	2.9	5.0	1.0	1.3
25	16 21 43	−50 28 27	1.0	3.3	1.2	8.5	5.9	7.8	2.1	1.7
26	16 22 30	−50 01 39	1.2	3.8	1.4	9.2	6.0	6.5	2.1	1.5
27	16 23 08	−50 01 03	1.0	2.5	1.0	8.4	5.2	7.1	1.8	1.9
28	16 22 02	−50 10 15	1.0	2.3	0.9	7.2	3.8	6.1	1.3	1.5
29	16 21 41	−50 11 51	1.2	3.1	1.2	6.9	5.8	5.9	2.0	1.7
30	16 20 30	−50 38 27	1.3	4.0	1.5	9.3	9.7	8.0	3.4	2.3
31	16 22 29	−50 06 51	1.3	4.7	1.8	5.0	5.5	4.4	1.9	1.1
32	16 20 17	−50 56 51	1.0	1.9	0.7	4.3	2.2	2.9	0.8	1.1
33	16 19 55	−51 04 03	1.2	3.3	1.3	7.1	5.7	5.9	2.0	1.6
34	16 20 08	−51 00 03	0.8	1.4	0.5	6.9	2.6	5.6	0.9	1.7
35	16 21 46	−50 27 27	1.0	2.9	1.1	11.1	6.0	9.4	2.1	1.9
36	16 20 55	−50 44 27	1.2	3.1	1.2	10.9	8.4	7.8	2.9	2.5
37	16 21 08	−50 15 15	0.7	0.7	0.3	5.9	1.5	5.0	0.5	1.9
38	16 22 55	−50 00 39	0.9	1.4	0.5	7.5	4.1	6.8	1.4	2.7
39	16 21 14	−50 33 51	1.1	2.5	0.9	10.1	6.5	7.8	2.3	2.5
40	16 21 49	−50 05 51	1.0	2.3	0.9	8.0	4.4	6.4	1.5	1.8
41	16 20 04	−51 00 39	0.7	1.1	0.4	5.8	1.9	5.0	0.7	1.6
42	16 22 42	−50 04 39	1.2	2.6	1.0	7.4	6.6	6.5	2.3	2.3
43	16 21 53	−50 00 03	1.2	2.6	1.0	4.9	3.8	4.1	1.3	1.3
44	16 20 30	−50 43 39	1.4	3.5	1.3	8.2	7.2	5.7	2.5	1.9
45	16 21 17	−50 41 15	1.0	2.4	0.9	8.7	5.2	7.7	1.8	2.0
46	16 20 53	−50 41 03	1.4	3.2	1.2	10.2	10.9	8.2	3.8	3.1
47	16 20 49	−51 00 27	0.8	1.2	0.4	3.5	1.2	2.5	0.4	0.9
49	16 21 06	−50 29 39	0.9	1.4	0.5	6.2	3.1	5.2	1.1	2.1
50	16 19 11	−51 06 39	1.0	1.3	0.5	5.8	3.2	4.9	1.1	2.2
52	16 19 32	−50 52 51	0.9	1.0	0.4	5.2	2.0	3.7	0.7	1.9
53	16 21 56	−50 10 51	0.8	1.3	0.5	7.4	3.3	6.8	1.1	2.3
54	16 21 00	−50 29 15	0.9	1.0	0.4	5.2	2.5	4.7	0.9	2.4
55	16 21 07	−50 31 51	0.8	0.9	0.4	8.4	3.4	7.4	1.2	3.4

Table 3 – continued

$N_{\text{mm}}$	mm-dust					$^{13}\text{CO}$				
	RA (h m s)	Dec. (d m s)	$R_{\text{mm}}$ (pc)	$S_{\text{mm}}$ (Jy)	$M_{\text{mm}}$ ( $10^3 M_{\odot}$ )	Peak ( $10 \text{ K km s}^{-1}$ )	Sum ( $10^3 \text{ K km s}^{-1}$ )	$N(^{13}\text{CO})$ ( $10^{16} \text{ cm}^{-2}$ )	$M_{^{13}\text{CO}}$ ( $10^3 M_{\odot}$ )	$M_{^{13}\text{CO}} : M_{\text{mm}}$
(1)	(2)	(3)	(4)	(5)	(6)	(7)	(8)	(9)	(10)	(11)
57	16 21 22	−50 43 15	1.1	1.5	0.6	7.2	4.8	5.6	1.7	2.9
59	16 21 54	−50 06 15	1.1	2.3	0.9	9.3	6.0	6.9	2.1	2.4
64	16 20 16	−51 03 27	1.1	1.5	0.6	6.0	4.3	5.2	1.5	2.6
65	16 21 49	−50 12 51	1.0	1.7	0.6	7.0	4.9	6.6	1.7	2.7
66	16 21 55	−50 34 51	1.3	2.0	0.8	8.4	8.0	7.1	2.8	3.7
67	16 21 53	−50 27 03	0.9	1.2	0.4	9.2	4.2	7.3	1.5	3.4
70	16 20 32	−50 50 03	0.9	1.0	0.4	5.0	2.3	4.0	0.8	2.1
72	16 22 15	−50 02 39	0.6	0.6	0.2	4.9	1.4	4.8	0.5	2.2
74	16 20 33	−50 33 39	0.9	1.1	0.4	7.2	4.0	6.7	1.4	3.3
75	16 21 42	−50 05 03	1.0	1.2	0.4	7.5	4.0	6.2	1.4	3.1
76	16 22 07	−50 02 51	0.8	0.8	0.3	5.4	2.5	5.1	0.9	2.8
79	16 22 01	−50 01 03	1.3	2.1	0.8	5.2	5.3	4.6	1.8	2.3
81	16 19 10	−51 09 27	0.6	0.4	0.2	4.8	1.2	4.2	0.4	2.6
82	16 22 28	−50 04 03	1.0	1.0	0.4	6.0	3.1	4.9	1.1	2.8
84	16 22 25	−49 59 03	0.7	0.5	0.2	4.1	1.3	3.7	0.4	2.4
85	16 20 04	−51 03 39	0.9	0.8	0.3	7.3	3.3	6.4	1.1	3.8
86	16 21 49	−50 19 15	1.3	1.8	0.7	8.9	8.7	7.1	3.0	4.4
87	16 20 32	−50 53 27	1.0	0.9	0.3	4.3	2.1	3.2	0.7	2.2
88	16 21 33	−50 18 51	0.8	0.6	0.2	6.2	2.3	5.6	0.8	3.5
89	16 20 35	−50 51 27	0.9	0.8	0.3	4.9	2.3	4.0	0.8	2.6
90	16 20 04	−50 58 39	0.8	0.8	0.3	7.0	2.7	5.9	0.9	3.0
93	16 20 57	−50 23 15	1.1	1.0	0.4	5.2	2.6	3.3	0.9	2.5
94	16 22 38	−50 06 03	0.9	0.8	0.3	5.8	3.0	5.0	1.0	3.4
95	16 21 21	−50 11 15	0.6	0.3	0.1	6.7	1.4	6.0	0.5	4.4
96	16 19 47	−51 07 39	1.1	1.2	0.4	4.9	3.0	3.5	1.1	2.5
97	16 21 04	−50 24 03	0.8	0.6	0.2	6.3	2.4	5.7	0.8	3.8
98	16 19 55	−50 57 03	1.0	1.0	0.4	4.3	2.3	3.3	0.8	2.1
99	16 21 58	−50 16 15	0.6	0.4	0.1	5.2	1.4	4.9	0.5	3.3
100	16 22 12	−50 28 03	0.7	0.4	0.1	6.2	1.7	5.7	0.6	4.3
104	16 22 22	−50 18 51	0.8	0.5	0.2	5.8	2.0	4.8	0.7	3.6
105	16 21 39	−50 20 15	0.8	0.4	0.2	8.7	3.1	7.4	1.1	6.5
106	16 22 47	−50 09 27	0.5	0.2	0.1	6.0	1.1	5.4	0.4	4.5
107	16 21 09	−50 41 39	0.8	0.6	0.2	7.7	3.4	6.9	1.2	5.7
108	16 21 55	−50 36 51	0.6	0.3	0.1	6.2	1.4	5.9	0.5	4.5
109	16 22 11	−50 21 03	0.7	0.4	0.2	7.1	2.2	6.3	0.8	5.0
110	16 22 17	−50 00 03	0.6	0.3	0.1	4.2	0.9	3.8	0.3	3.3
111	16 20 49	−50 27 27	0.6	0.3	0.1	5.1	1.3	4.9	0.4	4.3
113	16 21 57	−50 31 51	0.8	0.5	0.2	6.7	2.6	5.9	0.9	5.3
117	16 20 20	−51 00 03	0.8	0.5	0.2	4.9	1.9	4.0	0.7	3.3
119	16 21 53	−50 25 03	0.6	0.3	0.1	8.7	2.2	7.6	0.8	7.1
120	16 20 15	−50 41 15	0.6	0.2	0.1	6.2	1.2	4.9	0.4	4.7
121	16 21 02	−50 19 39	0.7	0.3	0.1	5.9	1.6	5.4	0.6	4.6
122	16 19 00	−51 08 15	0.6	0.2	0.1	4.8	1.0	4.3	0.4	3.8
123	16 21 14	−50 45 03	0.7	0.3	0.1	6.1	1.9	5.7	0.7	5.4
125	16 21 33	−50 39 27	0.9	0.6	0.2	6.5	3.6	6.3	1.3	5.9
128	16 20 21	−50 52 03	0.7	0.3	0.1	4.2	1.3	3.6	0.5	3.6
129	16 22 18	−50 20 39	0.6	0.2	0.1	5.7	1.2	4.8	0.4	5.1
132	16 21 48	−50 10 15	0.5	0.2	0.1	6.4	1.1	5.2	0.4	5.5
133	16 21 41	−50 32 15	0.8	0.5	0.2	8.2	3.8	7.8	1.3	7.5
135	16 22 19	−50 13 27	0.7	0.3	0.1	6.0	1.4	4.5	0.5	4.6
136	16 22 08	−50 25 39	0.6	0.2	0.1	7.1	1.5	6.7	0.5	7.8
138	16 22 22	−50 25 39	0.6	0.2	0.1	5.8	1.1	5.3	0.4	6.2

relationship between the gas and dust emission, we took the 105 mm-dust clump fits and measured the  $^{13}\text{CO}$  flux density from the GMC 2D moment image (with no clipping applied) in the areas defined by the 105 mm-dust clump fits. Table 3 gives the mm-dust clump fit properties and the associated  $^{13}\text{CO}$  measurements as well

as the equivalent total mass of each clump that was calculated from the gas and dust data using equations (2) and (3), respectively. The total masses of all the clumps found in this way are  $2.0 \times 10^5 M_{\odot}$  (gas) and  $2.2 \times 10^5 M_{\odot}$  (dust), with at least a factor of 2 error in each given the assumptions used and errors in the flux density scales.



**Figure 13.** Plots of the parameters derived from the 105 mm-dust clump fits. Top: mass–radius scatter plot, with a regression curve fit of  $M_{\text{mm}} \propto R_{\text{mm}}^{3.96 \pm 0.14}$ ; the limiting case of the beam radius at 3.6 kpc is indicated by the dotted line (middle) distribution of fitted clump radii; the limiting case of the beam radius at 3.6 kpc is indicated by the dotted line (bottom) mass spectrum with spectral index  $\alpha_M = 1.67 \pm 0.09$  fitted above the turnover; the dot-dashed line indicates the start of the bins used in the fit. The  $115 M_{\odot}$  completeness limit is indicated by the vertical dashed line.

These measurements are the same order of magnitude as the total mass estimated by Mookerjee et al. (2004) from the full-resolution 1.2-mm dust data: from their CLUMPFIND analysis they obtained  $1.0 \times 10^5 M_{\odot}$  and from GAUSSCLUMPS they measured  $1.5 \times 10^5 M_{\odot}$ . We reiterate here that using convolved-down data and a constant  $T_{\text{mm}}$  for all clumps has led us to obtain higher masses than theirs.

The two total masses we have measured from the same regions (defined by the 1.2-mm clump fits) using the gas and the mm-dust

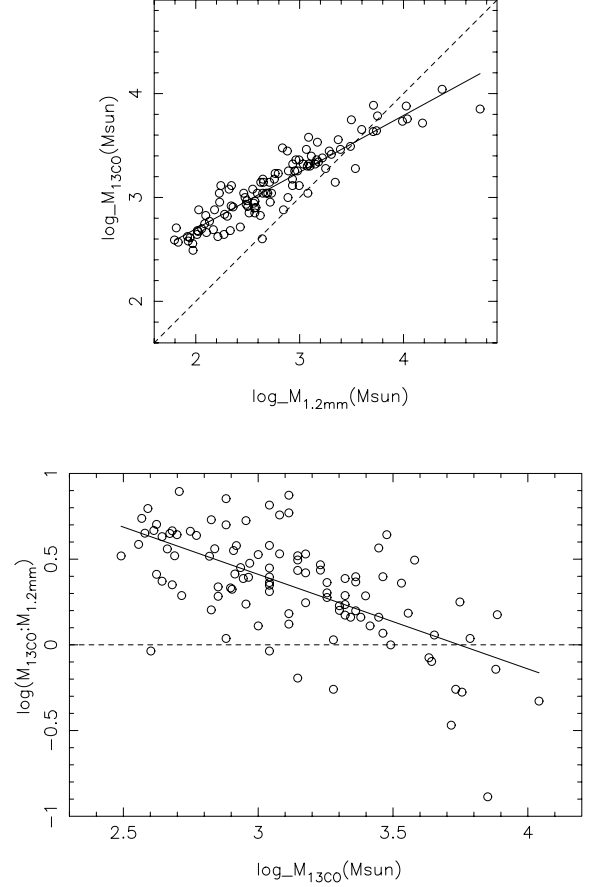


**Figure 14.** Top: the logarithmic relationship between the 105  $^{13}\text{CO}$  and mm-dust masses, measured from the respective images in the regions defined by the mm-dust clump fits. The regression curve fit shown corresponds to  $M_{^{13}\text{CO}} \propto M_{\text{mm}}^{0.55 \pm 0.02}$ ; the dotted line indicates  $M_{^{13}\text{CO}} = M_{\text{mm}}$ . Bottom: the variation of gas:dust mass ratio with  $^{13}\text{CO}$  mass measured in the same regions. The dotted line indicates a ratio of unity; the regression fit gives  $\frac{M_{^{13}\text{CO}}}{M_{\text{mm}}} \propto M_{^{13}\text{CO}}^{-0.55 \pm 0.07}$ .

data are in remarkable agreement, despite the assumptions we made. The dust absorption coefficient was assumed to be constant and LTE was assumed to derive the total  $^{13}\text{CO}$  column densities assuming optically thin emission. Therefore, this suggests that only a small fraction of the total gas mass is actually at hotter temperatures than 20 K. In Fig. 14, we show a scatter plot of the  $^{13}\text{CO}$  and mm-dust masses given in Table 3. The masses derived from the gas and dust do scale with each other, although it is not a one-to-one correspondence; a least-squares fit to the data gives  $M_{^{13}\text{CO}} \propto M_{\text{mm}}^{0.55 \pm 0.02}$ . An alternative way of showing the relationship is to plot the variation of gas:dust mass ratio (which should be unity if the assumptions are all correct) with gas mass for the  $^{13}\text{CO}$  measurements taken in the mm-dust clumps (Fig. 14). For the most part, the gas traces a larger mass than the dust, but the ratio diminishes as the gas mass increases, dropping to below unity mainly for the more massive clumps. The most likely explanation for this is that optical depth effects are higher in the more massive clumps, which we expect from our comparisons with the optically thin isotopomer  $\text{C}^{18}\text{O}$  (Section 4.1.3). Alternatively, the  $^{13}\text{CO}$  may be depleted in these clumps. This will be investigated with examination of the  $\text{C}^{18}\text{O}$  map.

In Fig. 15, we show how the  $^{13}\text{CO}$  masses vary as a function of the mm-dust clump radii they were measured from, and we

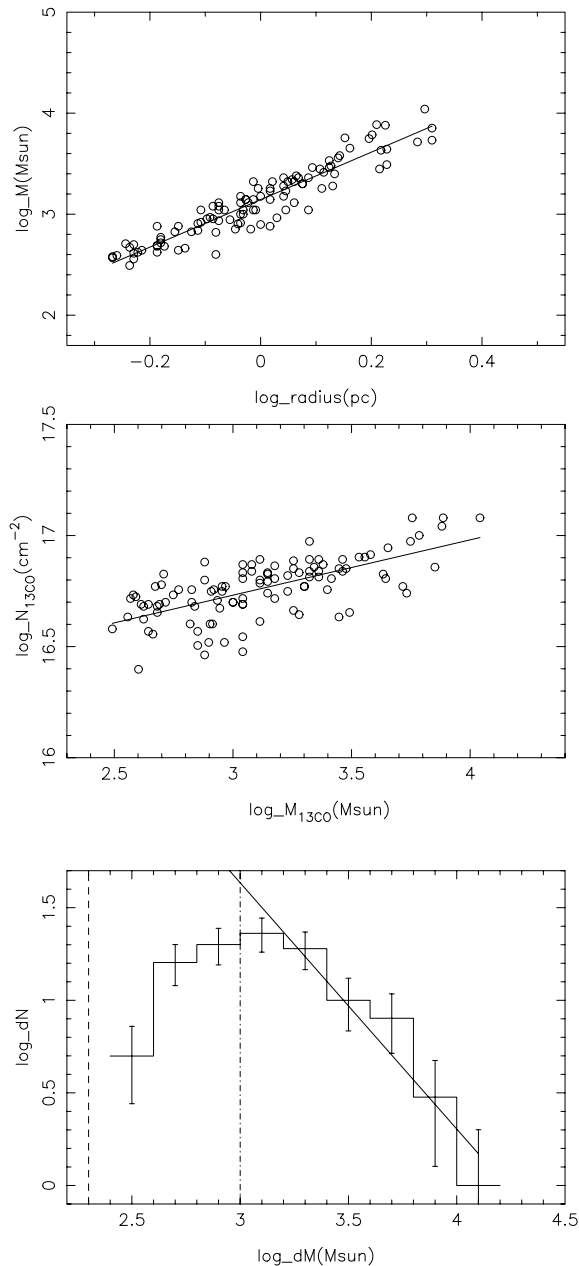


**Figure 15.**  $^{13}\text{CO}$  measurements taken from the regions defined by the 105 mm-dust clump fits. Top: the mass–radius relationship with a least-squares fit of  $M_{^{13}\text{CO}} \propto R_{\text{mm}}^{2.35 \pm 0.08}$ . Middle: the variation of column density as a function of clump mass  $N_{^{13}\text{CO}} \propto M_{^{13}\text{CO}}^{0.25 \pm 0.03}$ . Bottom: histogram of the  $^{13}\text{CO}$  masses; a fit to the spectrum above the turnover gives  $\alpha_M = 2.33 \pm 0.21$ ; the dot–dashed line indicates the start of the bins used in the fit. The dashed vertical line corresponds to the  $10\sigma$  mass estimate of  $200 M_{\odot}$  based on the  $1\sigma$  level of  $5 \text{ K km s}^{-1}$  on the zeroth moment image and a limiting clump size given by the beam size.

find a relationship of  $M_{^{13}\text{CO}} \propto R_{\text{mm}}^{2.35 \pm 0.08}$  which is interestingly in agreement with the mass–radius relationship found for the 61  $^{13}\text{CO}$  clumps (Section 4.1.1) and is again consistent with the Larson (1981) scaling law. The relation again suggests that in the regions sampled, the column density of the gas is close to constant, and from Table 3 this is indeed the case. This is shown graphically in the second plot of Fig. 15, in which  $N_{^{13}\text{CO}} \propto M_{^{13}\text{CO}}^{0.25 \pm 0.03}$ . The gas masses measured here also span a similar range to those sampled by the 61  $^{13}\text{CO}$  fits.

In Fig. 15, we also show the mass spectrum derived from the measurements taken from the  $^{13}\text{CO}$  data at the positions of the mm-dust clump fits. The fit above the turnover of  $\sim 10^3 M_{\odot}$  gives  $\alpha_M = 2.33 \pm 0.21$ , a slope that is consistent with, but much more robust than, that given by the mass spectrum constructed from the 61 CLUMPFIND fits to the  $^{13}\text{CO}$  data (Fig. 11). This is quantified by noting that varying the bin size by  $\sim \pm 10$  per cent results in a maximum change in  $\alpha_M$  of 7 per cent. The differences between the two  $^{13}\text{CO}$  mass spectrum plots can be explained by considering the dominant effect of the clump-like behaviour of the mm-dust, whose clump fits show a more normal distribution of radii (compare the bottom left plot of Fig. 11 with the middle plot of Fig. 13). If the gas column densities are relatively constant, then not only will the clump masses scale with radii, but the distribution of masses will be a function of the distribution of radii.

## 5 SUMMARY

A  $\sim 1 \text{ deg}^2$  region of the southern Galactic plane, centred on  $l \sim 333^\circ$ ,  $b \sim -0.5^\circ$ , has been mapped in  $^{13}\text{CO}$  using the new OTF mapping capability of the Mopra Telescope. Within the  $-120$ – $20 \text{ km s}^{-1}$  velocity bandpass sampled, the region contains five distinct velocity features with the dominant feature of interest centred on  $-50 \text{ km s}^{-1}$ . This feature is itself a complex of molecular clouds, containing sites of massive star formation, H II regions and bright dust emission. We have derived the properties of this complex by decomposing the 2D integrated  $^{13}\text{CO}$  structure into clumps and fitting to these using the CLUMPFIND algorithm of Williams et al. (1994). We found 61 clumps in the gas data, although generally speaking the gas structure appears non-clump-like and this is borne out by the clump mass spectrum which does not display a power-law behaviour.

We also fitted to dust data from the same region that we convolved-down to the resolution of our data: namely, 1.2-mm SEST and 21- $\mu\text{m}$  MSX images. We find that based on clump centre positions, within a beam size, only 50 per cent of the gas clumps have an associated dust clump at either wavelength. The gas and dust emission appear to trace different aspects of the GMC: the gas is extended and of low relative contrast between the brightest and faintest emission, whilst the dust traces compact structures and displays a much higher relative contrast.

The total LTE gas mass found from the 61 clump fits to the  $^{13}\text{CO}$  data is  $2.7 \times 10^5 M_{\odot}$ . The total dust mass found from the 105 clump fits to the convolved-down 1.2-mm SEST data is  $2.2 \times 10^5 M_{\odot}$  and the total LTE mass measured from the  $^{13}\text{CO}$  data in the regions of the mm-dust clump fits is  $2.0 \times 10^5 M_{\odot}$ .

In subsequent papers, we will detail the full 3D (i.e. including the velocity structure and linewidths) analysis of the  $^{13}\text{CO}$  data. The  $^{13}\text{CO}$  data forms the first part of an ongoing project to survey the same region in several molecular species that are sensitive to a range of density conditions, in order to investigate the role played by turbulence in star formation.

## ACKNOWLEDGMENTS

The Mopra Telescope is part of the Australia Telescope which is funded by the Commonwealth of Australia for operation as National Facility managed by CSIRO. The authors wish to thank Stuart Robertson for his help with the observations and telescope procedure. IB acknowledges a research grant from UNSW. TW acknowledges support from the ARC. The authors wish to thank the referee for their helpful comments. This research has made use of the SIMBAD data base, operated at CDS, Strasbourg, France, and

also NASA's Astrophysics Data System. We also used data products from the *MSX* satellite. Processing of these data was funded by the Ballistic Missile Defense Organization with additional support from NASA Office of Space Science. This also required use of the NASA/IPAC Infrared Science Archive, which is operated by the Jet Propulsion Laboratory, California Institute of Technology, under contract with NASA.

## REFERENCES

- André P., Ward-Thompson D., Barsony M., 2000, in Mannings V., Boss A. P., Russell S. S., eds, *Protostars and Planets IV*. Univ. Arizona Press, Tucson AZ, p. 59
- Ballesteros-Paredes J., Mac Low M., 2002, *ApJ*, 570, 734
- Batchelor R. A., Caswell J. L., Haynes R. F., Wellington K. J., Goss W. M., Knowles S. H., 1980, *Aust. J. Phys.*, 33, 139
- Bik A., Kaper L., Hanson M. M., Smits M., 2005, *A&A*, 440, 121
- Bourke T. L. et al., 1997, *ApJ*, 476, 781
- Bourke T. L., Myers P. C., Robinson G., Hyland A. R., 2001, *ApJ*, 554, 916
- Brand J., Blitz L., 1993, *A&A*, 275, 67
- Bronfman L., Alvarez H., Cohen R. S., Thaddeus P., 1989, *ApJS*, 71, 481
- Brunt C. M., 2003, *ApJ*, 583, 280
- Caswell J. L., Haynes R. F., Goss W. M., 1980, *Aust. J. Phys.*, 33, 639
- Caswell J. L., Vaile R. A., Ellingsen S. P., Norris R. P., 1995, *MNRAS*, 274, 1126
- Crutcher R. M., 1999, *ApJ*, 520, 706
- Frerking M. A., Langer W. D., Wilson R. W., 1982, *ApJ*, 262, 590
- Gillespie A. R., Huggins P. J., Sollner T. C. L. G., Phillips T. G., Gardner F. F., Knowles S. H., 1977, *A&A*, 60, 221
- Hartmann L., Ballesteros-Paredes J., Bergin E. A., 2001, *ApJ*, 562, 852
- Hatchell J., Richer J. S., Fuller G. A., Quattrone C. J., Ladd E. F., Chandler C. J., 2005, *A&A*, 440, 151
- Heithausen A., Bensch F., Stutzki J., Falgarone E., Panis J. F., 1998, *A&A*, 331, L65
- Heyer M. H., Brunt C. M., 2004, *ApJ*, 615, L45
- Hill T., Burton M. G., Minier V., Thompson M. A., Walsh A. J., Hunt-Cunningham M., Garay G., 2005, *MNRAS*, 363, 405
- Johnstone D., Di Francesco J., Kirk H., 2004, *ApJ*, 611, L45
- Karnik A. D., Ghosh S. K., Rengarajan T. N., Verma R. P., 2001, *MNRAS*, 326, 293
- Kavars D. W., Dickey J. M., McClure-Griffiths N. M., Gaensler B. M., Green A. J., 2003, *ApJ*, 598, 1048
- Klein R. I., Fisher R. T., Krumholz M. R., McKee C. F., 2003, in Arthur J., Henney W., eds, *Rev. Mex. Astron. Astrofis. Ser. Conf. Vol. 15, Winds, Bubbles and Explosions: A Conf. to Honour John Dyson*. UNAM, Mexico, p. 92
- Klessen R. S., 2002, *Proc. ESO Workshop, The Origins of Stars and Planets: the VLT View*. ESO, Garching, p. 61
- Klessen R. S., Heitsch F., Mac Low M., 2000, *ApJ*, 535, 887
- Kraemer K. E., Shipman R. F., Price S. D., Mizuno D. R., Kuchar T., Carey S. J., 2003, *AJ*, 126, 1423
- Kramer C., Stutzki J., Rohrig R., Corneliussen U., 1998, *A&A*, 329, 249
- Ladd N., Purcell C., Wong T., Robertson S., 2005, *Pub. Astron. Soc. Aust.*, 22, 62
- Larson R. B., 1981, *MNRAS*, 194, 809
- Larson R. B., 2003, *Rep. Prog. Phys.*, 66, 1651
- Lazarian A., Pogosyan D., 2000, *ApJ*, 537, 720
- Lockman F. J., 1979, *ApJ*, 232, 761
- Mac Low M.-M., Klessen R. S., 2004, *Rev. Mod. Phys.*, 76, 125
- McClure-Griffiths N. M., Green A. J., Dickey J. M., Gaensler B. M., Haynes R. F., Wieringa M. H., 2001, *ApJ*, 551, 394
- Mestel L., Spitzer L., 1956, *MNRAS*, 116, 503
- Mizuno N. et al., 2003, in Burton M., Jayawardhana R., Bourke T., eds, *Proc. IAU Symp. 221, Star Formation at High Angular Resolution*. Astron. Soc. Pac., San Francisco, p. 226
- Mookerjee B., Kramer C., Nielbock M., Nyman L.-Å., 2004, *A&A*, 426, 119
- Mookerjee B., Kramer C., Burton M. G., 2005, in Wilson A., ed., *ESA SP-577. The Dusty and Molecular Universe: a Prelude to Herschel and ALMA*. ESA Publications Division, Noordwijk, p. 391
- Ossenkopf V., Mac Low M. M., 2002, *A&A*, 390, 307
- Padoan P., Boldyrev S., Langer W., Nordlund A., 2003, *ApJ*, 583, 308
- Retallack D. S., Goss W. M., 1980, *MNRAS*, 193, 261
- Rodgers A. W., Campbell C. T., Whiteoak J. B., 1960, *MNRAS*, 121, 103
- Rosolowsky E. W., Goodman A. A., Wilner D. J., Williams J. P., 1999, *ApJ*, 524, 887
- Russeil D., Adami C., Amram P., Le Coarer E., Georgelin Y. M., Marcelin M., Parker Q., 2005, *A&A*, 429, 497
- Scalo J. M., 1986, *Fundam. Cosmic Phys.*, 11, 1
- Shaver P. A., Goss W. M., 1970, *Aust. J. Phys. Astrophys. Suppl.*, 14, 133
- Shu F. H., Adams F. C., Lizano S., 1987, *ARA&A*, 25, 23
- Simon R., Jackson J. M., Clemens D. P., Bania T. M., Heyer M. H., 2001, *ApJ*, 551, 747
- Tafalla M., Myers P. C., Caselli P., Walmsley C. M., Comito C., 2002, *ApJ*, 569, 815
- Vázquez-Semadeni E., García N., 2001, *ApJ*, 557, 727
- Williams J. P., de Geus E. J., Blitz L., 1994, *ApJ*, 428, 693

This paper has been typeset from a  $\text{\TeX}/\text{\LaTeX}$  file prepared by the author.